N O T I C E

THIS DOCUMENT HAS BEEN REPRODUCED FROM MICROFICHE. ALTHOUGH IT IS RECOGNIZED THAT CERTAIN PORTIONS ARE ILLEGIBLE, IT IS BEING RELEASED IN THE INTEREST OF MAKING AVAILABLE AS MUCH INFORMATION AS POSSIBLE

The Pennsylvania State University

Electrical Engineering Department

University Park, Pennsylvania 16802

SECONDARY ELECTRON EMISSION FROM A CHARGED DIELECTRIC IN THE PRESENCE OF NORMAL AND OBLIQUE ELECTRIC FIELDS

Technical Report

NASA Grant No. NSG-3166

Bahram Javidi

February 1982

(NASA-CR-168558) SECONDARY ELECTRON EMISSION FROM A CHARGED DIELECTRIC IN THE PRESENCE OF NORMAL AND OBLIQUE ELECTRIC FIELDS M.S. Thesis (Pennsylvania State Univ.) 110 p HC A06/MF A01 CSCL 09C G3/33 N82-18507 Unclas 09166

The Pennsylvania State University

Electrical Engineering Department

University Park, Pennsylvania 16802

SECONDARY ELECTRON EMISSION FROM A CHARGED DIELECTRIC IN THE PRESENCE OF NORMAL AND OBLIQUE ELECTRIC FIELDS

Technical Report

NASA Grant No. NSG-3166

Bahram Javidi

February 1982

The Pennsylvania State University

The Graduate School

Department of Electrical Engineering

Secondary Electron Emission from a Charged Dielectric in the Presence of Normal and Oblique Electric Fields

A Thesis in

Electrical Engineering

by

Bahram Javidi

Submitted in Partial Fulfillment
of the Requirements
for the Degree of

Master of Science

March 1982

I grant The Pennsylvania State University the nonexclusive right to use this work for the University's own purposes and to make single copies of the work available to the public on a not-for-profit basis if copies are not otherwise available.

Bahram Javidi

We approve the thesis of Bahram Javidi.

Date of Signature:

1-15-82

Dale M. Grimes, Professor of Electrical Engineering, Head of the Department of Electrical Engineering

Lynn A. Carpenter, Associate Professor of Electrical Engineering

1-15-82

James W. Robinson, Professor of Electrical Engineering, Chairman of Committee, Thesis Adviser

ABSTRACT

The secondary electron emission coefficient was obtained for a FEP-Teflon dielectric charged with monoenergetic electrons normally incident upon the surface of the specimen. Measurements of secondary emission coefficient were done for normal and oblique incidence with different primary beam energies in the presence of normal and oblique electric fields.

The dielectric specimen was mounted on a flat stainless steel platform which was located inside a cylinder. The platform could be rotated by a stepper motor to make oblique measurements possible. Particle trajectories which deflected away from the specimen could be located with detector wires mounted on the cylinder, which could also be rotated. This data was analyzed by computer simulations to find the potential distribution on the surface of the specimen and the electric field around it. Furthermore, these computer simulations determined the impact point and the impact energy of the beam when, during secondary emission measurements, it struck the specimen. The system's alignment was checked by finding the platform position that corresponded to normal incidence using the two types of measurements mentioned above and comparing experimental and simulated data.

The experimental data were taken by setting the platform to different positions. Then a collimated probing beam was directed to different points on the surface of the specimen and the released or accumulated charge was monitored using an electrometer connected to the metalized coating on the back of the specimen. The measured data for different probing beam energies, different impact points and

different angles of incidence were plotted vs. impact energy and impact point. Also, the normal and tangential electric fields were obtained for different points on the surface of the specimen.

A brief review of classical secondary emission theory and straggle theory is presented. The straggle theory matches well with experimental results in regions having negligible electric field. Also, an empirical modification of this theory can match the experimental results in the presence of normal electric field; however, in the presence of tangential electric field the data depart from the values of secondary emission coefficient predicted by theory.

TABLE OF CONTENTS

Page

ABSTRACT iii

LIST OF TABLES vii

LIST OF FIGURES viii

LIST OF SYMBOLS xi

ACKNOWLEDGMENTS xv

Chapter

I. INTRODUCTION 1

A. Secondary Emission Theory 4

B. Straggle Theory 7

C. Straggle Theory Including Angle of Incidence 12

D. Summary 15

II. EXPERIMENTAL SYSTEM 17

A. The Dielectric Specimen 17

B. Flood Gun 19

C. Probe Beam 19

D. Detector Wires 21

E. Deflection Factor 21

F. Pulse Circuit 24

G. Charging and Discharging of the Specimen 27

H. Faraday Cup 33

I. Noise 36

J. Signal Monitoring System and Filters 40

III. MATHEMATICAL MODELING OF THE SYSTEM 44

A. Measuring the Surface Potential 47

B. Particle Trajectories (non-impacting) 49

TABLE OF CONTENTS (Concluded)

		Page
	C. Determination of V_D and Pl_r	55
IV.	SECONDARY EMISSION MEASUREMENTS	60
	A. Calculation of Secondary Emission Coefficient	60
	B. Procedure to Find σ	61
	C. Measurement of σ for Normal Incidence (uncharged specimen)	63
	D. Measurement of σ for Normal Incidence (charged specimen)	65
	E. Asymmetric Potential Distribution	67
	F. Calculation of σ Predicted by Theory and Curves of Measured Data Vs. Impact Energy	68
V.	SECONDARY ELECTRON EMISSION IN PRESENCE OF ELECTRIC FIELD	81
	A. Electric Field on the Surface	81
	B. Measurements of σ Near the Edges (Oblique Field)	81
	C. Measurements of σ in Regions with Normal Field	83
	D. An Analysis of Experimental Procedures	87
	E. An Analysis of Measured Data	90
REFERENCES		92

LIST OF TABLES

Table		Page
1	Surface Potential at the Center for Different Flood Gun Voltages	51
2	Cylinder Position, Deflection Voltage and Current in the Detector Wire for a Sample Deflection Measurement	54

LIST OF FIGURES

Figure		Page
1	Geometry used to model the system mathematically	3
2	The energy distribution of secondary electrons for tungsten	6
3	Representation of the energy dissipation as a function of depth for the straggle theory	8
4	Number of primary electrons as a function of depth	10
5	Representation of oblique incidence	13
6	Parts of the experimental system inside the vacuum chamber	18
7	Picture of the platform and the specimen	20
8	Geometry used to calculate the deflection factor D . . .	23
9	Representation of reflected trajectory and corresponding angles	25
10	Pulse circuit	26
11	The RC circuit and it's output	28
12	The output of the timer circuit	29
13	The output stage of the pulse circuit	30
14	The light source installation	32
15	The Faraday Cup	34
16	The Collector Cup	35
17	The first Cup design that didn't work	37
18	Noise added to the pulse	39
19	The monitoring devices	41
20	LPF1 and control box	42
21	Geometry of the conformal mapping	45
22	The normalized potential distribution on the surface of the specimen	48

LIST OF FIGURES (Continued)

Figure		Page
23	Illustration of the electrometer's response vs. the beam's voltage when surface potential is being measured	50
24	Plot of simulated and experimental exit angle for the case when the probe gun is centered above the specimen	57
25	Plot of simulated and experimental exit angle for different platform positions	58
26	Plot of σ for normal incidence with an uncharged specimen .	64
27	Plot of σ vs. deflection voltage for different platform positions and 11-kV beam energy	66
28	Platform tilted to achieve asymmetric potential distribution	69
29	Plots of σ for two cases of symmetric and asymmetric potential distribution	70
30	Geometry used to calculate angle	72
31	End points of range R´ vs. platform position pl_p	74
32	Plots of surface potential V(x) and impact angle θ_{imp} vs. simulated deflection voltage. The measured deflection voltage is drawn on a lower scale	75
33	Plots of measured σ and σ predicted by the theory vs. deflection voltage	77
34	Plots of σ vs. impact energy for different beam energies. The angle of incidence θ' is between 0° and 20°	78
35	Plots of σ vs. impact energy for different beam energies. The angle of incidence θ is between 20° and 40°	79
36	Plots of σ vs. impact energy for different beam energies. The angle of incidence θ' is between 40° and 60°	80
37	X and Y component of electric field on the surface of the specimen	82
38	Plots of σ vs. impact point for different beam energies. The angle θ' is between 0° and 20°	84

LIST OF FIGURES (Concluded)

Figure		Page
39	Plots of σ vs. impact point for different beam energies. The angle θ' is between 20° and 40°	85
40	Plots of σ vs. impact point for different beam energies. The angle θ' is between 40° and 60°	86
41	Representation of the situation when the beam is striking near the edge	88
42	Representation of the situation when the beam is almost lost	89
43	Plots of σ vs. impact point for experimental data and theory	91

LIST OF SYMBOLS

β	The deflection angle.
δ	The true secondary electron coefficient.
δ_m	The maximum value of true secondary electron coefficient.
θ_{imp}	The angle at which the particle strikes the specimen.
θ_{in}	The angle that locates the effective source point of the beam.
θ'_{in}	Corrected angle that locates the injection point.
θ_{out}	The angle that locates the exit point of the beam.
θ'	The angle at which the particle strikes the specimen with respect to the normal to the surface of the specimen.
τ	The pulse width.
σ	The total secondary electron emission coefficient.
σ_m	The maximum value of the total secondary electron emission coefficient.
ϕ	The angle of inclination relative to the radius.
ϕ'	Corrected angle of inclination.
a	The radius of the cylinder.
A_n	Coefficients of potential polynomial.
B	The transformed value of B_s in the Z plane.
B_s	The half width of the specimen.
c	The correction term which arises because the beam is deflected before it enters the cylinder.
C	A constant depending on the type of material.
Cyl_p	Cylinder position.
Cyl_r	Cylinder reference position.
D	The angle between the beam and the normal to the cylinder surface per unit voltage between the deflection plates.
e	The electrical charge equal to 1.6×10^{-19} C.
E	The energy loss of a primary electron in the target.

LIST OF SYMBOLS (Continued)

E_c	The critical energy that corrosponds to unity secondary electron emission coefficient.
E_{imp}	The impact energy of the primary electron.
E_u	The u component of the electric field in the W plane.
E_v	The v component of the electric field in the W plane.
E_x	The x component of the electric field in the Z plane.
E_y	The y component of the electric field in the Z plane.
f(x)	The probability function for a secondary to escape from the target.
$H_n(z)$	A function used to find the universal yield curve.
I	The beam current.
I(A)	Current in the detector wire.
K	A constant depending on the type of material.
L	The length of the half cylinder.
L_s	The length of the platform.
LPF1	Low pass filter number one.
LPF2	Low pass filter number two.
n	The exponent which is used to approximate the range of particles travelling through the sample.
n_o	Number of primary electrons at the surface of the sample.
n(x)	The number of secondaries produced in the sample.
N	The degree of the surface potential polynomial.
N(E)	Number of secondaries produced as a function of their energy.
$P(x,E_{imp})$	The probability that a primary with initial energy E_{imp} travels some distance x through the sample.
Pl_p	The platform position.
Pl_r	The platform position for which the incident beam is normal to the specimen.

LIST OF SYMBOLS (Continued)

Q_c	The charge collected by the Cup.
Q_s	The charge released by the specimen.
R	The maximum distance that a primary travels through the sample.
R	The range of the deflection voltage.
s,t	The real and imaginary parts of $\frac{dZ}{dW}$.
T_1	The transistor that drives transistor T_2 in the pulse circuit.
T_2	The transistor that is either cut-off or saturated in the pulse circuit.
U,V	Real and imaginary parts of W.
V	The impulse produced by the switch circuit of the pulse generator.
V_0	The center surface potential.
V_1,V_2	Deflection voltages for which edges of the specimen are detected.
V_D	The correction deflection voltage.
$V_{D.C.}$	The beam's energy.
$V_{Def.sim.}$	The deflection voltage used in simulation.
$V_{Def.data}$	The measured deflection voltage.
V_{high}	The high voltage of the pulse circuit.
V_{low}	The low voltage of the pulse circuit.
V_{out}	The output of the pulse circuit.
V_x	The velocity of the particle in the x direction.
V_y	The velocity of the particle in the y direction.
V(x)	The potential on the surface of the specimen.
V(X,Y)	The potential of a point (x,y) in the Z plane.
W	Complex representation of points inside the semi-circle.
x	Electron path into the dielectric specimen.

LIST OF SYMBOLS (Concluded)

x,y	A point in the z plane.
z	A parameter porportional to impact energy.
Z	The complex plane that represents the upper half plane.
Z_m	The value of Z that gives the maximum value of δ.

ACKNOWLEDGMENTS

The author wishes to express his thanks to Dr. James W. Robinson, who supervised this work and from whom he learned much. He also appreciates the financial support provided by the National Aeronautics and Space Administration under Grant NSG-3166.

I. INTRODUCTION

The surface of a spacecraft is often covered with dielectrics which are exposed to charged particles. In vacuum, charged particles accumulate on these insulators, sometimes making a potential of up to a few kV. Unfortunately, the charge distribution on the spacecraft body is not uniform. As a result, flashovers are created between different points on the spacecraft. The arcing can cause different problems, such as eroding of surface materials or resetting the logical circuits inside the spacecraft. This is frequently observed in our experiments when flashovers inside the vacuum chamber have reset the logical circuit of the stepper motor. Reduction of the flashovers requires a study of these dielectrics and their behavior when subjected to charged fluxes in vacuum. Previous studies(1-8) have been related to this problem.

When a dielectric specimen is exposed to a monoenergetic beam of electrons, the surface charge which is established depends primarily on the accelerating voltage and the geometry of the specimen(1,2,3). J. W. Robinson(1,2,3) developed a technique for measuring surface charge distribution without placing any measuring apparatus near the face of the sample. It was found out that the potential is nearly flat around the center of the specimen and it falls sharply around the edges. His results for FEP-Teflon dielectric are given in (2).

These results were used by N. Quoc-Nguyen(6) to calculate the potential distribution on the surface of the specimen and fields around it by a combination of a conformal mapping and an integration of a two-dimensional Green's function. He obtained the effects of normal electric fields on the secondary electron emission coefficient for a dielectric

specimen with different surface charges. According to his results, critical energy, which is the energy that yields a unity secondary emission coefficient, increases as electric field gets stronger.

It was not possible to measure secondary emission coefficient with an oblique angle of incidence in the system used by Quoc-Nguyen. Also, his system was hard to analyze mathematically. Therefore, it was necessary to design a new system so that measurements could be made for different angles of incidence and the system could be presented in a simple mathematical form.

A system to suit these goalswas a grounded half cylinder which could be rotated in front of a probing beam. The dielectric specimen was placed on a flat platform which was located in the center of the horizontal plane. This is shown in Figure 1. The dielectric can be charged with another source and, because of the special geometry of the system, the charge distribution on the surface allowed for both normal and oblique electric fields to be present. This charge distribution is estimated by finding particle trajectories shaped by the environment using a computer simulation of the experimental system(7). These simulations calculate fields, generate trajectories, and find equipotential lines.

This new system was used by P. A. Budd(8) to do secondary emission measurements for a dielectric which was charged with a normal electron beam. Measurements at oblique angles were done mostly near the center of the specimen where the field was normal.

The work reported here is an extension of previous works and it has been mainly concerned with finding fields and secondary emissions using normally and obliquely incident electrons near the edge of the

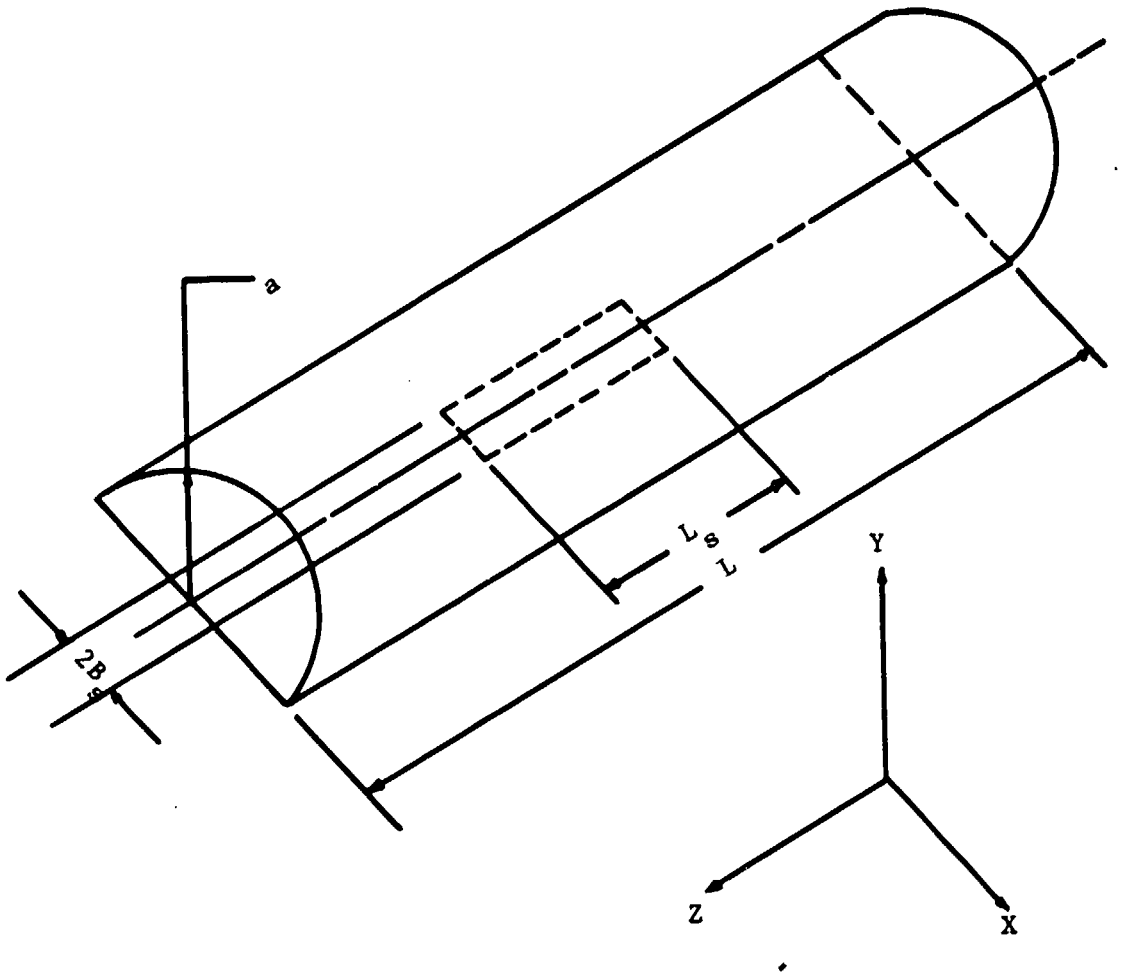

Figure 1. Geometry used to model the system mathematically. Note that $L = 2.5\ L_s$

specimen where field was not normal. These measurements are compared with values predicted by straggle theory which is modified to account for normal electric field. This is done because the value of critical energy changes in regions with strong electric fields. Furthermore, the expression for the secondary emission coefficient predicted by theory can be simplified by considering only particles with high impact energy.

A. Secondary Emission Theory

There are different theories concerning secondary emission phenomena. One of these theories is the straggle theory which is used by other people and it has shown a good match with experimental results in regions with a negligible electric field(9). Furthermore, a modified version of this theory was used in previous work(8) in regions with a normal electric field and it has matched the experimental results. Therefore, the straggle theory is used in this work. A brief review of secondary emission theory has to be considered.

When a target is bombarded by electron beams, it emits electrons. For some range of the electron beam's energy, the number of electrons that leave the target's surface may be larger than the number of incoming electrons. The incident electrons are called primary electrons and the emitted electrons are called secondary electrons. Electrons that leave the surface are divided into three categories, those primaries which are reflected elastically, those which are reflected with some loss of energy, and those electrons which were originally in the target. This third category of electrons have obtained sufficient energy from the primaries to escape from the target(10).

A typical energy distribution of secondaries, taken from Dobretsov (11), is shown in Figure 2. The ordinate N(E) is the number of secondaries produced and E is the primary energy. Three peaks {1, 2, 3} correspond to the three categories of electrons mentioned above namely, elastic, inelastic and secondaries, respectively.

In this report, the secondary emission coefficient σ is defined to be the ratio of all electrons that leave the surface to the number of primaries. This coefficient depends on the primary electron energy, temperature of the surface, pressure, cleanness, the angle of incidence, the work function and the potential distribution on the surface. For many conditions, the true secondary emission is nearly the same as the sum of the three types. Thus the theory used is that for true secondary emission(11). The number of true secondaries produced is given theoretically by

$$\delta = \int n(x) f(x) dx \tag{1}$$

where $n(x)dx$ is the number of secondaries produced in the layer x, x+dx by a primary and where $f(x)$ is the probability for those secondaries produced to escape from the target(12). The range of the integral is the thickness of the sample.

It is assumed that $n(x)$ is proportional to the change of energy of the primary as it travels through the sample or

$$n(x) = - K\frac{dE}{dx} \tag{2}$$

The probability function $f(x)$ is given by an exponential absorption law:

$$f(x) = e^{-\alpha x} \tag{3}$$

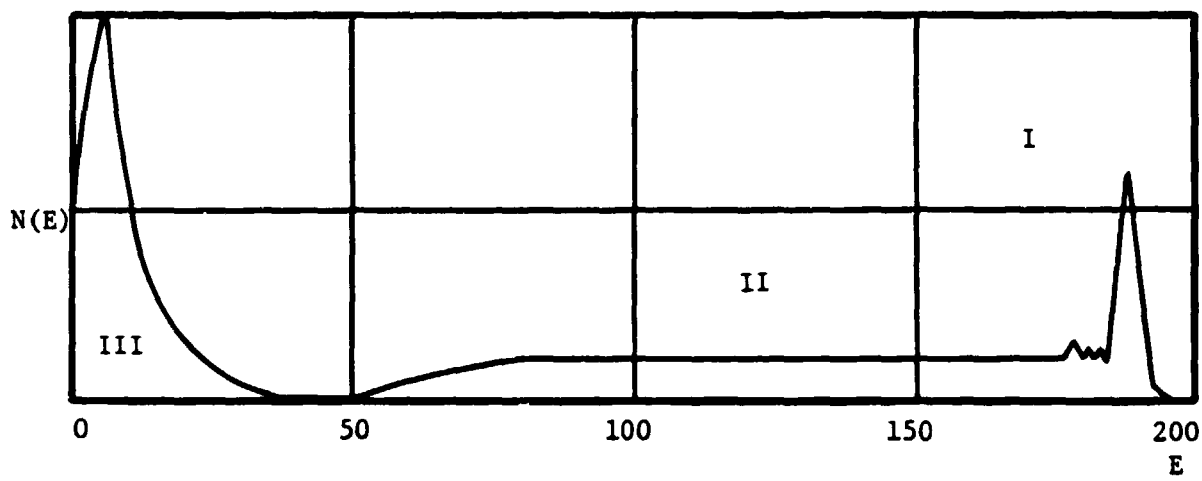

Figure 2. The energy distribution of secondary electrons for tungsten.

B. Straggle Theory

Among different theories presented for secondary emission phenomena, this theory agrees well with experimental results except that it does not predict field effects. It was originally presented by R. G. Lye and A. D. Dekker(13).

The theory basically assumes that the energy of primaries is equalized over the range that primaries travel through the sample. Accordingly, the energy loss is constant over the range and is given by (9,14,15,16)

$$\frac{dE}{dx} = - \frac{E_{imp}}{R} \tag{4}$$

where E_{imp} is the impact energy of a primary and R is the range.

According to elementary theory, the number of secondaries produced in the sample is

$$n(x) = - K \frac{dE}{dx} \tag{5}$$

from which is obtained the result, as shown in Figure 3, that

$$n(x) = K \frac{E_{imp}}{R} , \quad 0 \leq x \leq R \tag{6}$$

This result occurs because the number of primaries decreases linearly with distance as they travel through the sample. This can be put into the following mathematical form:

$$P(x, E_{imp}) = 1 - x/R \tag{7}$$

where $P(x, E_{imp})$ is the probability that a primary with initial energy E_{imp} travels some distance x through the sample. This can be shown by

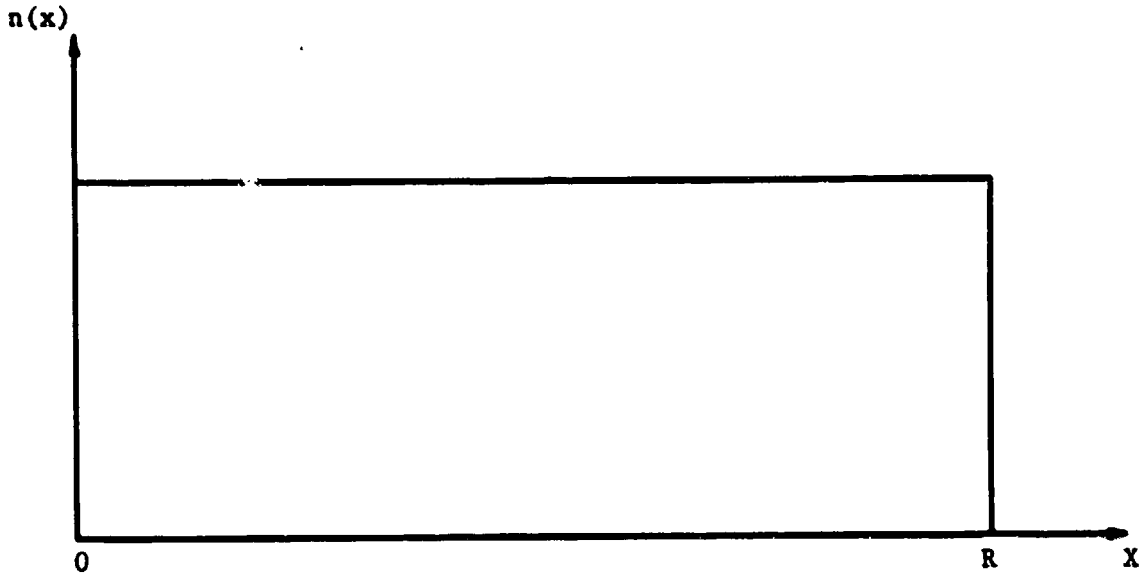

Figure 3. Representation of the energy dissipation as a function of depth for the straggle theory.

Figure 4.

This theory assumes that the primary range R is proportional to the initial energy E_{imp} raised to some power, as shown by

$$R = CE_{imp}^{n+1} \tag{8}$$

where constants C and n depend on the type of material.

According to the straggle theory, the secondary emission coefficient δ may be calculated from Equations 1, 2, 3, and 6 to be

$$\delta = \int_0^R \frac{KE_{imp}}{R} e^{-\alpha x} dx = \frac{KE_{imp}}{\alpha R}[1 - e^{-\alpha R}] \tag{9}$$

When equation 8 is true, then the expression for δ is

$$\delta = KE_{imp} \frac{1 - \exp(-\alpha CE_{imp}^{n+1})}{\alpha CE_{imp}^{n+1}} \tag{10}$$

When the impact energy is high, the exponential part in Equation 10 is negligible and δ becomes

$$\delta = \frac{K}{\alpha CE_{imp}^{n}} \tag{11}$$

This can be written in the following form:

$$\delta = \left(\frac{E_c}{E_{imp}}\right)^n \tag{12}$$

where n is some number depending on the type of sample used and the critical energy E_c is the energy that corresponds to a unity secondary coefficient $\delta = 1$.

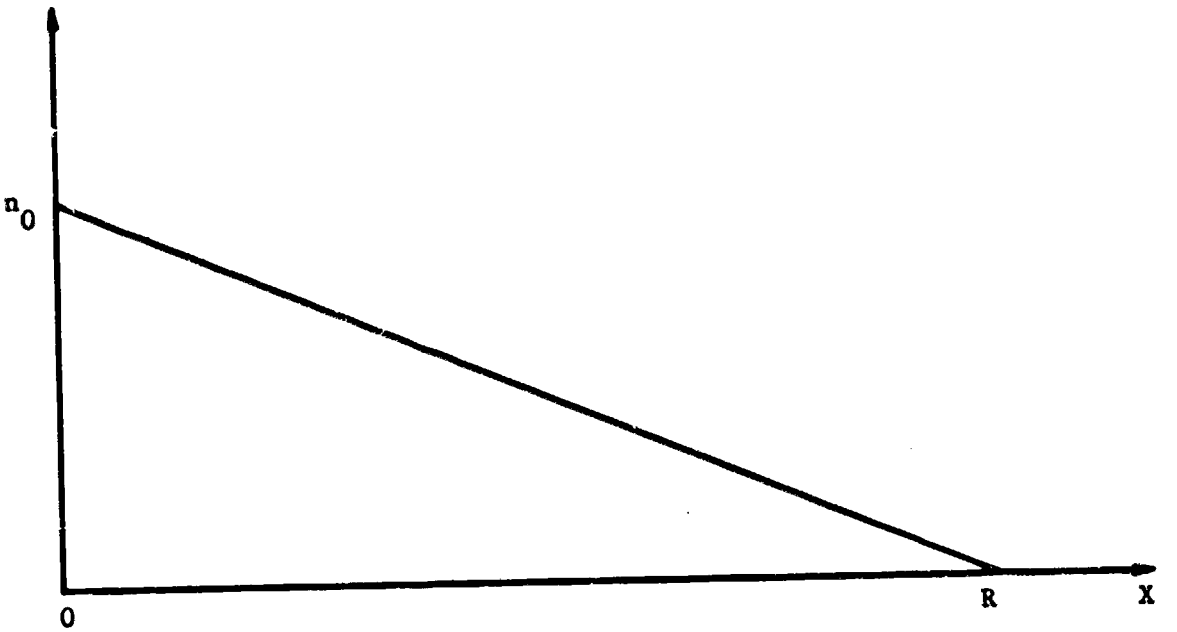

Figure 4. Number of primary electrons as a function of depth.

The secondary emission coefficient δ in Equation 10 can be rewritten(10) by assuming that

$$H_n(z) = \frac{1 - \exp(-z^{n+1})}{z^n} \tag{13}$$

where

$$z = (\alpha C)^{\frac{1}{n+1}} E_{imp} . \tag{14}$$

Equation 10, after some manipulation, then becomes

$$\delta = K (\alpha C)^{-\frac{1}{n+1}} H_n(z) . \tag{15}$$

The maximum value of δ is found by differentiating Equation 15 and setting it to zero to find the corresponding z. This value of z called z_m is substituted into Equation 15 to find the secondary coefficient δ_m

$$\delta_m = K H_n(z_m)(\alpha C)^{-\frac{1}{n+1}} \tag{16}$$

where z_m is given by

$$z_m = (\alpha C)^{\frac{1}{n+1}} E_m . \tag{17}$$

Dividing δ in Equation 15 by δ_m in Equation 16 and substituting z and z_m as shown in Equations 14 and 17, the following form is obtained:

$$\delta/\delta_m = \frac{H_n(E_{imp}\ z_m/E_{imp\ m})}{H_n(z_m)} . \tag{18}$$

The Equation 18 is a universal reduced yield curve.

C. Straggle Theory Including Angle of Incidence

Experiments have shown that secondary coefficient δ increases for primaries with oblique angles of incidence(17). The reason is that secondaries produced are closer to the surface and there is a stronger probability that they escape. This can be understood better by considering Figure 5. In this case, the probability function becomes

$$f(x) = e^{-\alpha x \mathrm{Cos}\theta'} \tag{19}$$

where the mean path has changed from x to $x\mathrm{Cos}\theta'$ (18). By looking at the probability function we observe that it has increased compared to $f(x) = e^{-\alpha x}$ for the normally incident case.

As usual, the number of secondaries produced is

$$n(x) \sim -\frac{dE}{dx} \, . \tag{20}$$

According to the main assumption in straggle theory, the energy loss is constant and is given by

$$\frac{dE}{dx} = -\frac{E_{imp}}{R} \, . \tag{21}$$

Therefore,

$$n(x) = K \frac{E_{imp}}{R} \tag{22}$$

where R is the range and it is equal to CE_{imp}^{n+1}. The equation given in elementary theory for σ yields

$$\delta(x) = \int_0^R f(x)\, n(x)\, dx \, . \tag{23}$$

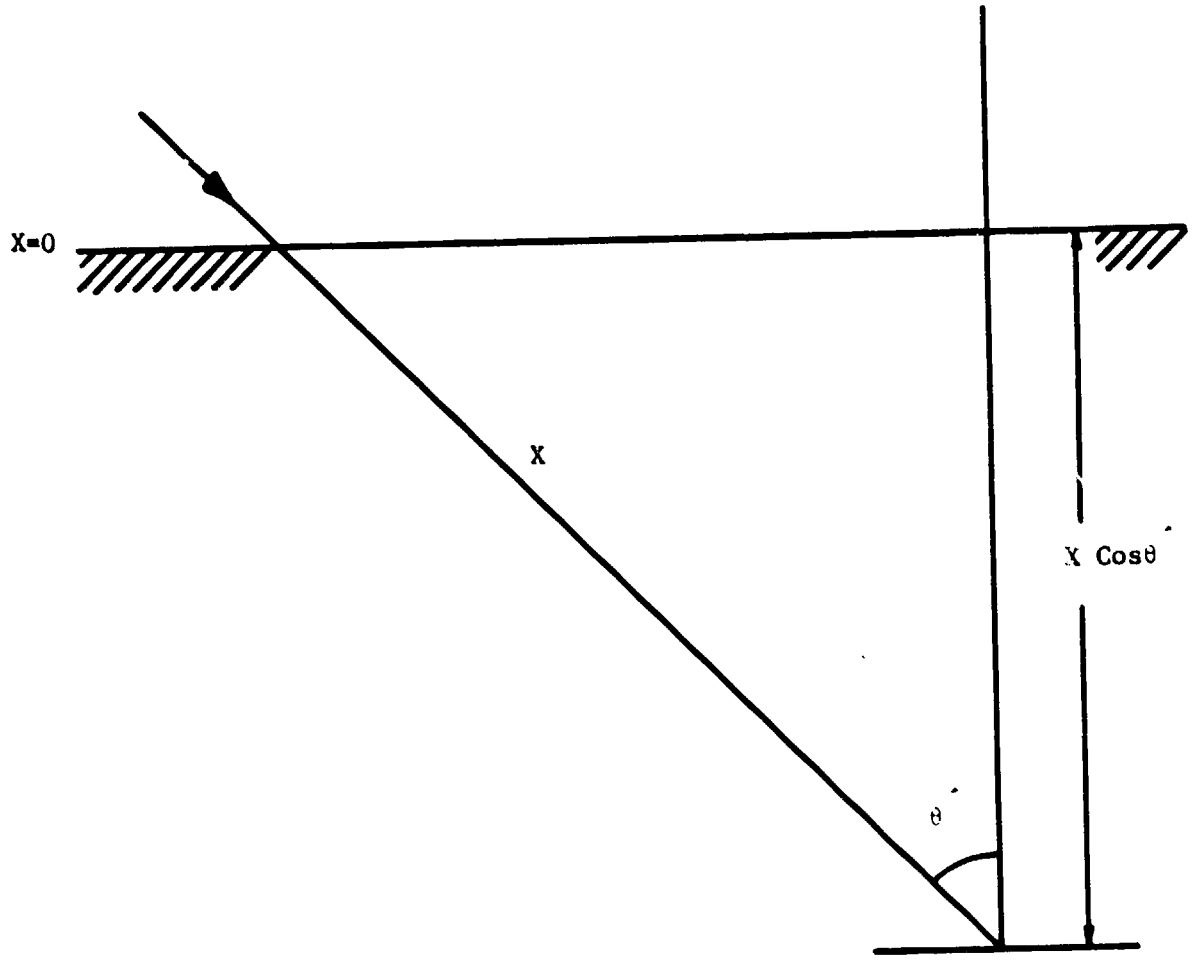

Figure 5. Representation of oblique incidence.

Substituting Equations 19 and 22 in 23, we have

$$\delta(x) = \int_0^R K \frac{E_{imp}}{R} e^{-\alpha x \cos\theta'} dx \tag{24}$$

which, after some manipulation, yields

$$\delta = \frac{KE_{imp}}{R\alpha\cos\theta'} (1 - e^{-\alpha R\cos\theta'}) . \tag{25}$$

Since $R = CE_{imp}^{n+1}$(13), δ becomes

$$\delta = \frac{KE_{imp}}{C\alpha\cos\theta' E_{imp}^{n+1}} (1 - e^{-\alpha R\cos\theta'}) \tag{26}$$

or

$$\delta = \frac{K}{C\alpha\cos\theta' E_{imp}^{n}} (1 - e^{-\alpha C\cos\theta' E_{imp}^{n+1}}) . \tag{27}$$

When the primary energy E_{imp} is high, the exponential term in the above equation becomes negligible and δ becomes

$$\delta = \frac{K}{\alpha E_{imp}^{n}} \frac{1}{\cos\theta'} \tag{28}$$

This can be put into the form

$$\delta = \left(\frac{E_c}{E_{imp}}\right)^n \frac{1}{\cos\theta'} \tag{29}$$

which is similar to Equation 12 except that it is multiplied by the factor $\frac{1}{\cos\theta'}$. The two parameters E_c and n are as defined in Equation 12 for the normally incident case. According to Equation 29, the ratio of δ for two different angles is

$$\frac{\delta(\theta_1')}{\delta(\theta_2')} = \frac{\cos\theta_2'}{\cos\theta_1'} \tag{30}$$

Again as it was done for normal incidence in the last section, a universal yield curve can be found by assuming that

$$H_n(z) = \frac{1 - \exp(-z^{n+1})}{z^n} \tag{31}$$

where

$$z = (\alpha C \mathrm{Cos}\theta')^{\frac{1}{n+1}} E_{imp} \cdot \tag{32}$$

Using Equations 31 and 32 in Equation 27 gives

$$\delta = K(\alpha C \mathrm{Cos}\theta')^{-\frac{1}{n+1}} H_n(z) \cdot \tag{33}$$

The value of z that maximizes $H_n(z)$ is z_m and the corresponding δ is δ_m. Therefore, δ_m becomes

$$\delta_m = K(\alpha C \mathrm{Cos}\theta')^{-\frac{1}{n+1}} H_n(z_m) \cdot \tag{34}$$

The ratio δ/δ_m can be found by dividing Equation 33 by Equation 34 as follows.

$$\delta/\delta_m = \frac{1}{H_n(z_m)} H_n(z_m E_{imp}/E_{imp\ m}) \cdot \tag{35}$$

This agrees with the universal yield curve(10).

D. Summary

Secondary electron emission is the phenomena by which electrons are emitted from a solid bombarded by charged particles. There are different theories governing this phenomena and most of them give similar results. The straggle theory was presented in this chapter

because its modified form has matched the experimental result of previous work(8).

According to this theory, the expression to determine δ for normal incidence is given by Equation 10 and the expression to determine δ for oblique incidence is given by Equation 27. When the impact energy is more than 1.5 kV, Equations 10 and 27 reduce to Equations 12 and 29. The values of δ calculated by these approximate forms are compared to experimental values of δ in Chapter IV.

II. EXPERIMENTAL SYSTEM

This chapter describes different parts of the experimental system which are used in this work. The main structure of the system is unchanged from what was explained by P. Budd(8). However, some significant changes made the system easier to use and less noisy.

The basic system as shown in Figure 6 was inside a 45 cm diameter stainless steel jar. Hard vacuum inside the jar was achieved by using a turbomolecular pump and all measurements were done at a pressure below 10^{-6} torr. The dielectric specimen was mounted on a grounded stainless steel platform which was located inside a grounded cylinder with an opening as shown in Figure 6. The cylinder and platform were rotated by stepper motors which were located outside the jar. Each motor step corresponded to 1.8°.

A. The Dielectric Specimen

The dielectric specimen was a piece of .125 mm FEP-teflon material which was covered on its backside by a metal coating. The specimen was located on a flat stainless steel platform and it was covered by a thin sheet of stainless steel which had an opening in the middle. This opening defined the rectangular piece of dielectric that was to be tested.

The metalized coating was cut into two parts by a slit which had a width of about 0.3 mm. It was made as narrow as possible so that the field around the slit wouldn't be disturbed. The purpose of the slit was to calibrate the deflection voltage of the beam. It also determined how wide the beam was. The slit was made about .7 mm from the center of the specimen.

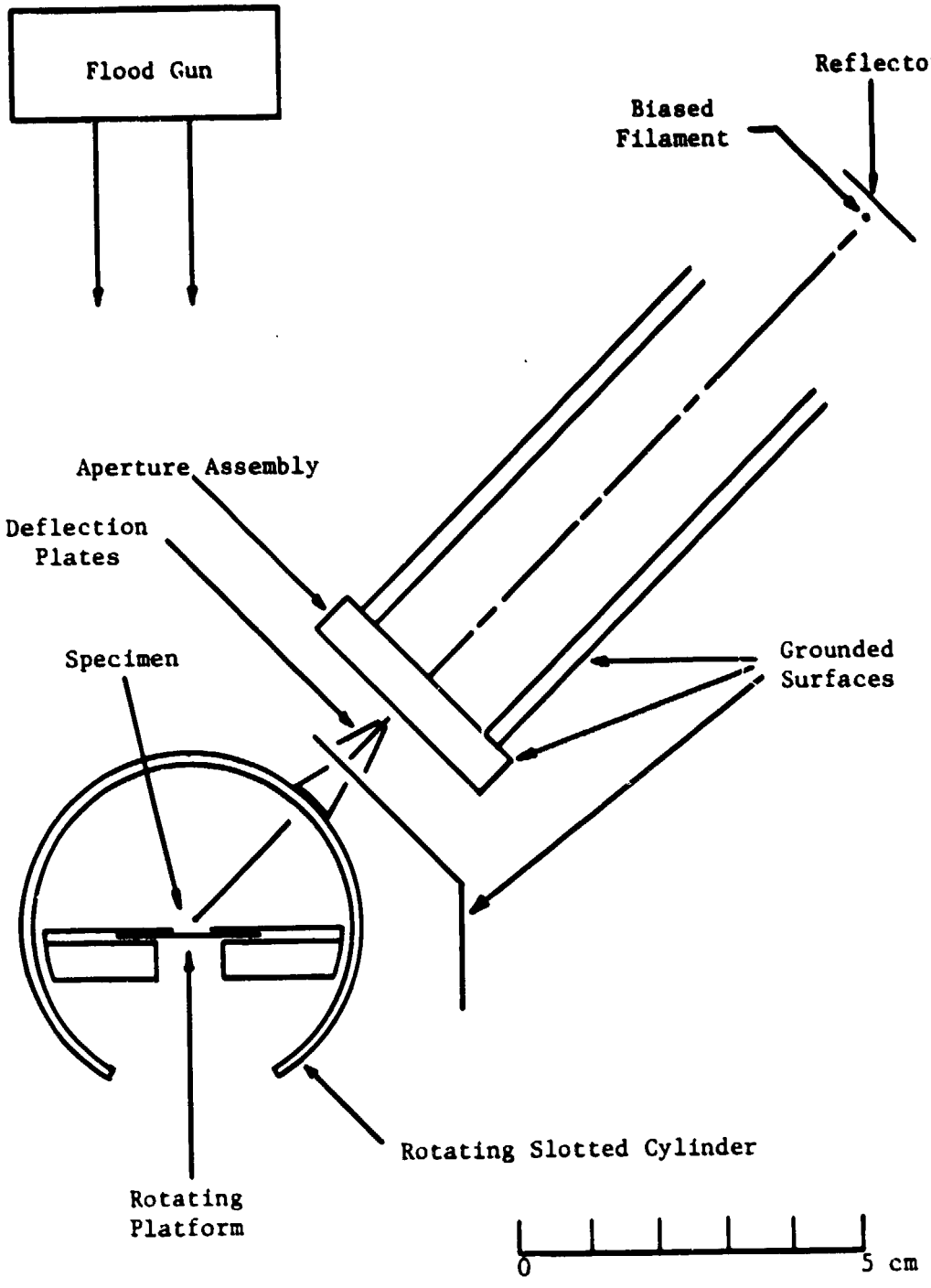

Figure 6. Parts of the experimental system inside the vacuum chamber.

A picture of the specimen, platform, cover sheet and the slit is shown in Figure 7. Since the platform was grounded, the back metalized portion of the specimen was insulated from it by another dielectric sheet. Two cuts were made in this insulator dielectric and two wires which passed through these cuts connected the two parts of the metal coating to two pins outside the vacuum system.

B. Flood Gun

The charging of the sample was done using the flood gun which consisted of a tungsten wire and accelerating electrodes. It was capable of producing a broad electron beam which could cover the whole specimen and charge up all the points on the surface of the specimen simultaneously. A high voltage power supply in the range of 0 to 30-kV was used to accelerate electrons produced from the tungsten wire toward the specimen.

C. Probe Beam

Another feature installed in the system was a collimated electron beam. The dimensions of the beam which passed through a slit were about .15 mm x 1 mm(8). These were much smaller than dimensions of the flood gun beam. The beam was produced from a tungsten filament and electrons were accelerated using the same power supply used for the flood gun beam. Since the filament was fixed at two points, there was some kind of stress on the filament because it would expand when it was turned on and it would contract when it was turned off. This stress caused the filament to break frequently and it had to be replaced. In order to avoid this breakdown, one end of the filament

ORIGINAL PAGE
BLACK AND WHITE PHOTOGRAPH

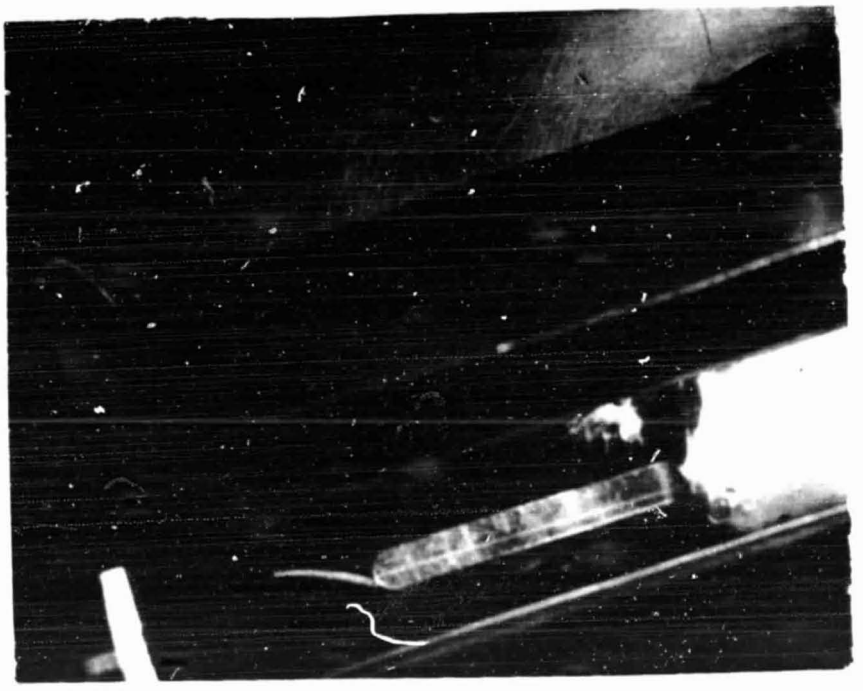

Figure 7. Picture of the platform and the specimen. The line on the specimen is the slit.

was left loose so that the expansion and contraction wouldn't cause breakage.

The probing beam passed between two deflection plates so that the beam could impact the specimen at different angles and different positions. Anytime the filament was replaced, there was a shift in the deflection voltages corresponding to different points on the specimen because the new filament was not placed exactly as the old one was. This shift could be calculated using the deflection factor D (rad/V) as will be explained in a later section.

The probe beam was used when the window of the cylinder was turned away from the specimen. Thus, the beam could not have approached the specimen except that a slot had been cut in the cylinder to admit the beam. This slot had a length of more than half the circumference of the cylinder.

D. Detector Wires

There were four detector wires located outside the cylinder slot, but mounted so that they would turn with the cylinder. Therefore, it was possible to detect where the beam entered and left the cylinder by rotating the cylinder until one of the wires intercepted the beam. Detector wires were used to conduct reflected-trajectories experiments as explained in Chapter III.

E. Deflection Factor

It's necessary to introduce the deflection factor D here. It's defined as the angle between the beam and the normal to the cylinder surface per unit voltage between the deflection plates. Therefore, it has the units of radians per volt.

The deflection factor D was determined as explained here. Two electrometers were connected to the two back sections of the specimen. Then a beam having a certain energy was directed toward the platform. When a change of deflection voltage caused the beam to pass over an edge of the specimen, the electrometer current changed. Thus, the deflection voltages corresponding to the slit and the outside edges were detected.

The deflection factor D was calculated from the geometry of Figure 8. In this figure, the distance a between the specimen and the point where the beam enters the cylinder is added to the correction term c which arises because the beam is deflected before it enters the cylinder. The radius is 2.54 cm and the correction term is considered to be 1.0 cm which is the distance between the cylinder and point of deflection(8). The half-width B_s of the specimen is 3.25 mm and the deflection angle β is calculated from

$$\beta = \tan^{-1} \frac{B_s}{a+c} \tag{36}$$

As a last step the deflection factor D is determined by dividing 2β by the deflection voltage that sweeps the beam across the specimen.

As an example, when the beam energy is 9.5 kV the edges of the specimen are detected at 430 V and -660 V. Therefore, D is

$$D = 1.67 \times 10^{-4} \text{ rad/V} \tag{37}$$

The deflection factor D for a beam with an energy of E is

$$D = \left(\frac{9.5}{E}\right)(1.67 \times 10^{-4}) \text{ rad/V} \tag{38}$$

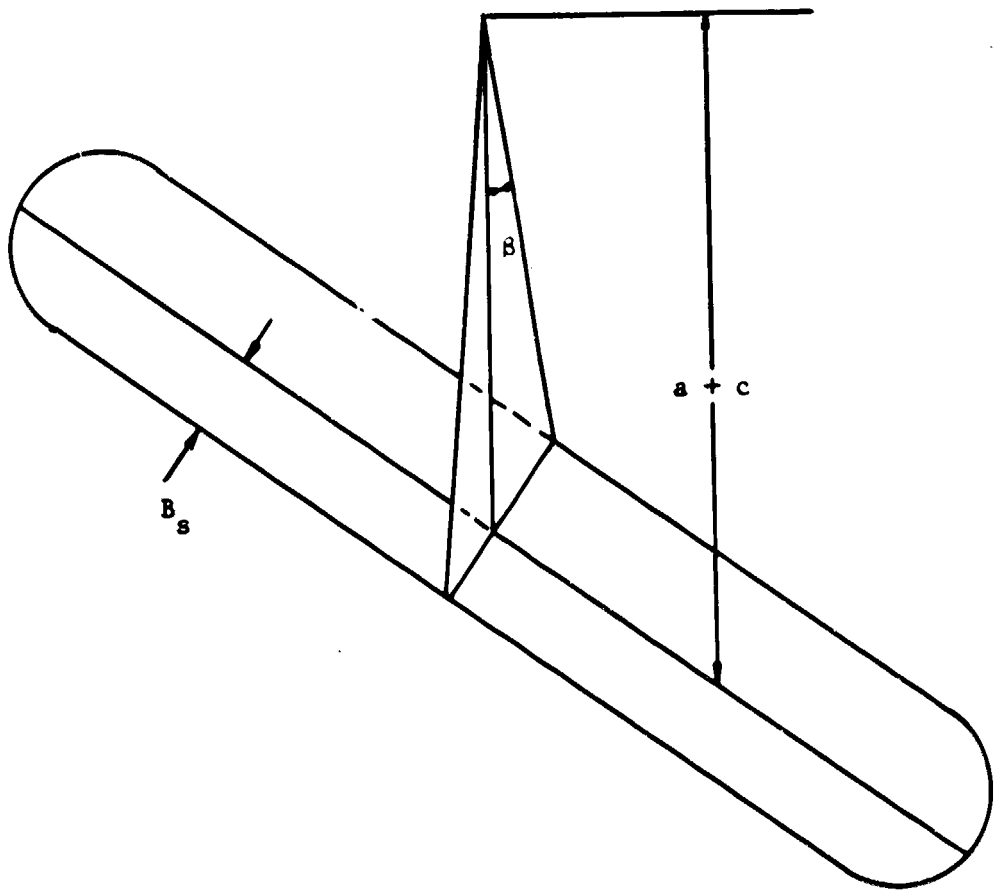

Figure 8. Geometry used to calculate the deflection factor D.

Because the beam is deflected at a point outside the cylinder, a correction factor has to be considered. Figure 9 shows the geometry used to calculate the correction factor. The angle ϕ is the angle of inclination relative to the radius and θ_{in} locates the effective source point of the beam. Using trigonometric relationships, we can obtain

$$\phi' = -1.4\phi \quad \text{and} \tag{39}$$

$$\theta'_{in} = \theta_{in} + .4\phi \tag{40}$$

where ϕ' is the corrected angle of inclination relative to the radius and θ'_{in} is the corrected angle that locates the injection point as shown in Figure 9.

In this calculation, it was assumed that ϕ is small enough so that $\sin \phi \simeq \phi$.

F. Pulse Circuit

When the specimen was charged prior to the recording of data, the probe-beam had to be kept away from the charged specimen. Otherwise, the beam would change the potential distribution on the surface. At the same time, it was desired to hit the specimen with the beam for secondary measurements. Thus, it was necessary to design a pulse circuit to deflect the beam to different points on the specimen during the measurements. When no pulse was triggered, the beam hit the platform and not the specimen. This circuit is shown in Figure 10.

The circuit contained a positive 5 volts power supply and several different stages were designed to generate the pulse. The first stage was an RC circuit designed such that by pushing a switch an impulse was

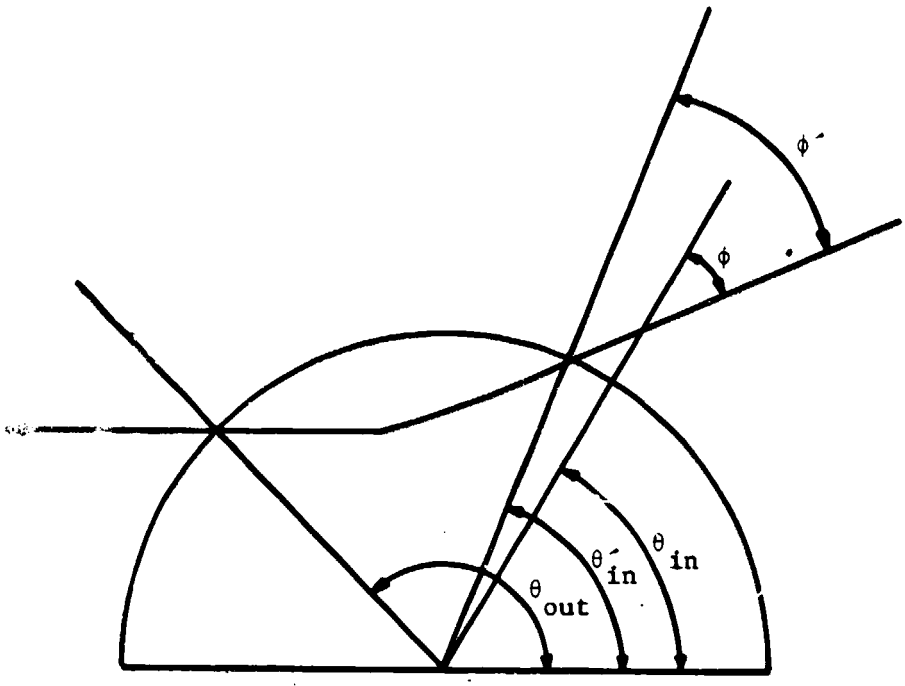

Figure 9. Representation of reflected trajectory and corresponding angles.

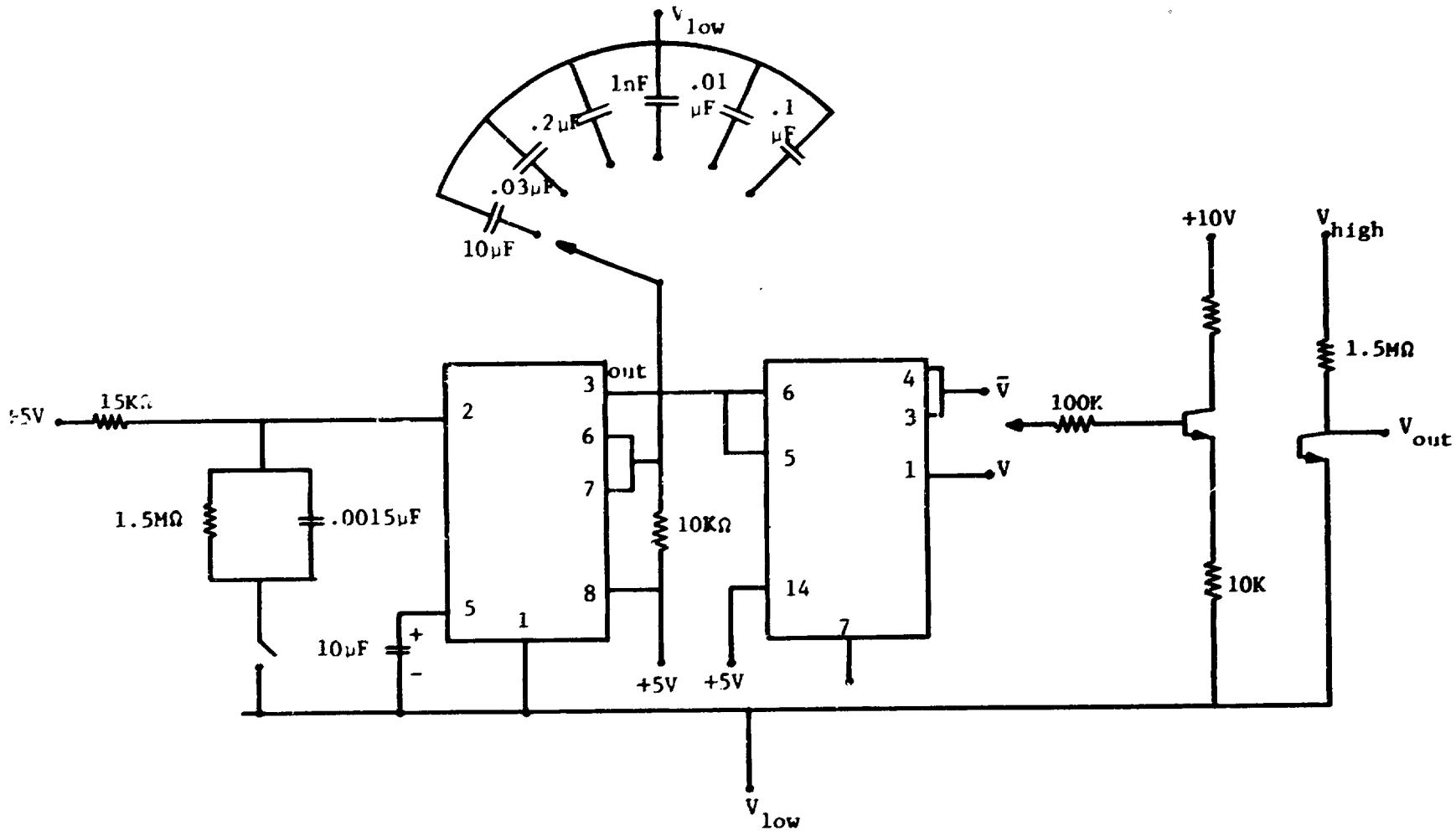

Figure 10. Pulse circuit.

produced as shown in Figure 11.

The next stage of the pulse circuit was a reliable bounceless pulse generator which was achieved by using a 555 timer connected for monostable operation. The impulse was applied to the input of the timer circuit and a mono stable pulse was produced as shown in Figure 12. The width of the pulse τ was determined by a discharge capacitor c. A range of pulse width τ from .1 ms to1.5s was provided by locating six different capacitors in the circuit. The pulse width then was selected by switching its corresponding capacitor into the circuit. The pulse generated in the 555 timer circuit was passed through two consecutive inverters from which both the pulse and its inverse were available.

The pulse then was applied to the last stage which is shown in Figure 13. Transistor T_1 amplified current so that T_2, was either cut off or saturated. Therefore, V_{out} was either V_{high} or V_{low}. Gain was adjusted so that the lower part of the pulse was flat and the transitions were sharp. The collector of T_2 was connected to one of the deflection plates and the other deflection plate was grounded.

If V_{high} was high enough, then the beam hit the platform and it did not discharge the specimen. Different points on the specimen could be hit by setting V_{low} to different voltages and by triggering the pulse generator.

G. Charging and Discharging of the Specimen

The charging of the specimen was done using the flood gun which was previously described. During the process of charging, the opening of the cylinder faced upward and the platform was horizontal so the

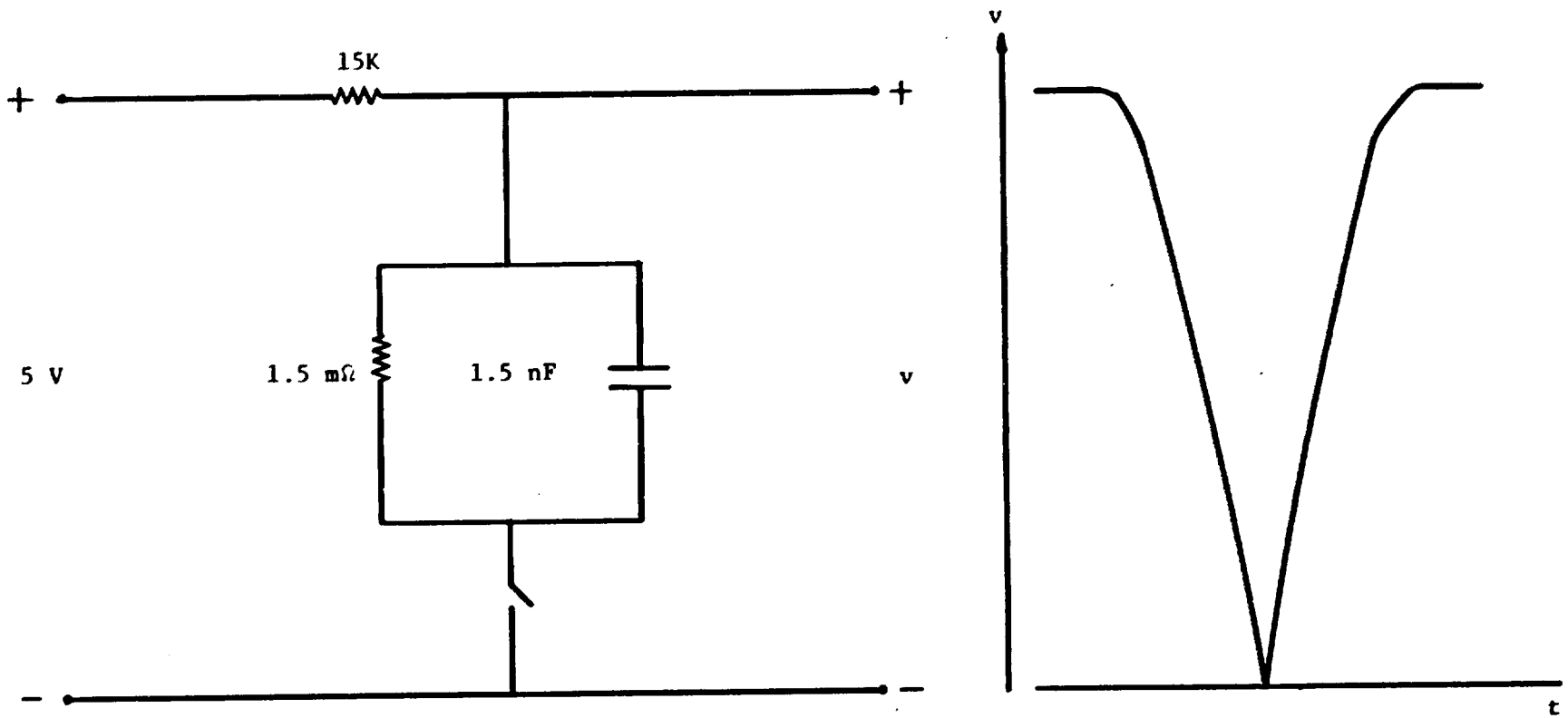

Figure 11. The RC circuit and its output.

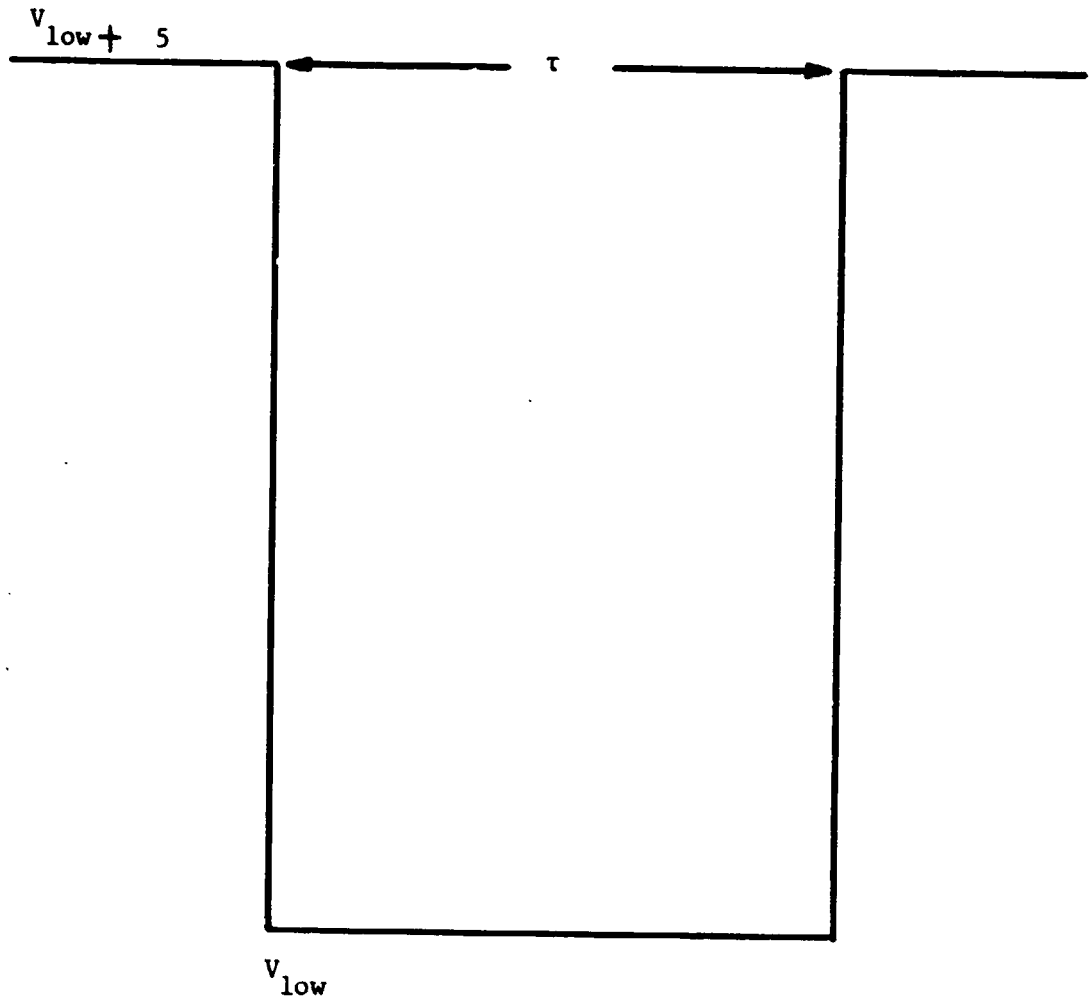

Figure 12. The output of the timer circuit.

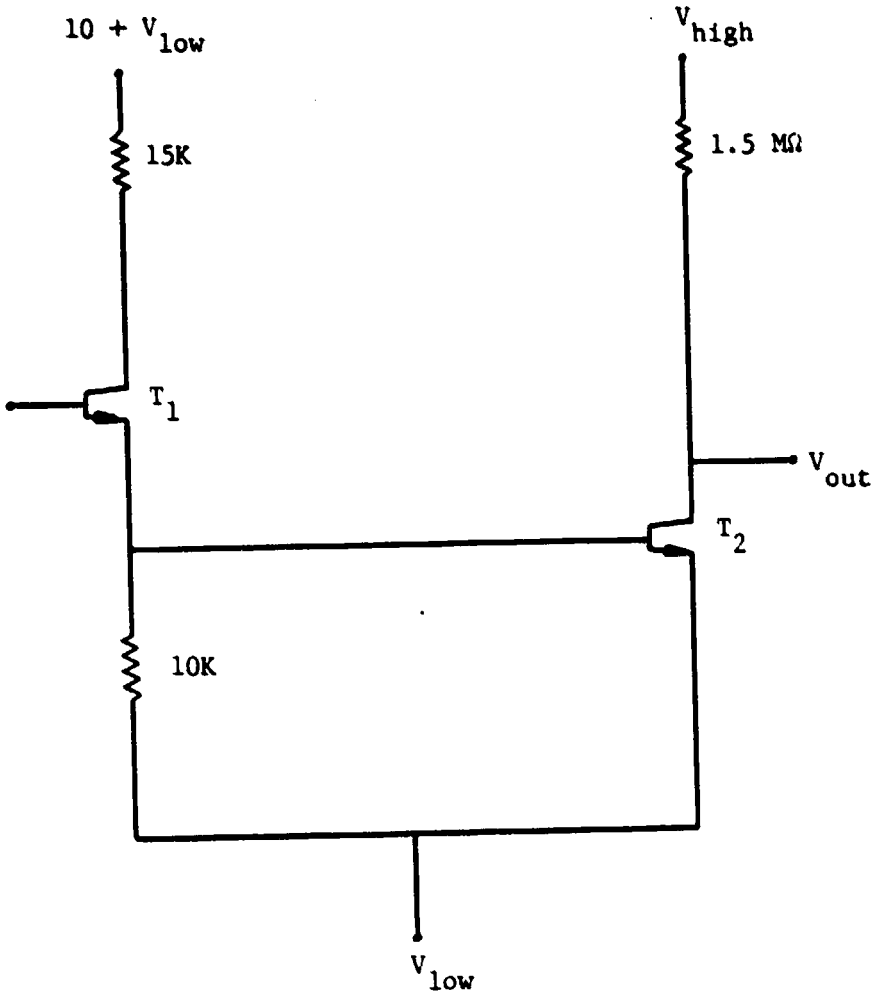

Figure 13. The output stage of the pulse circuit.

flood gun beam could hit the specimen at normal incidence. After the specimen surface was bombarded with these high energy electrons, the filament current was turned down and the cylinder was rotated until the opening faced downward.

A similar procedure could be used to discharge the specimen. In this case, the filament was turned on and the platform was set at a horizontal position so that the beam could hit the specimen at normal incidence. The power supply was turned to a high voltage and then it was slowly turned to zero.

The reason why the specimen charges when the voltage is increased is that when the impact energy of primaries is larger than the critical energy, the secondary emission coefficient is less than one according to Equation 12. Therefore, the number of electrons that are leaving the surface is less than the number of electrons that are hitting the surface. As a result, the specimen charges up.

When the impact energy of primaries is less than the critical energy, with a similar reasoning, more electrons are leaving the surface than hitting the surface and the specimen discharges. This is the case when voltage is turned down.

At some point, it was decided to try an ultra-violet light source for discharging purposes. The photons would give enough energy to the electrons on the surface of the specimen that they would escape from their bounds and leave the surface. For this purpose a source was installed on top of the box that contains the flood gun filament. A hole was made on the top face of the box so that the high energy beam could reach the specimen. This design is shown in Figure 14.

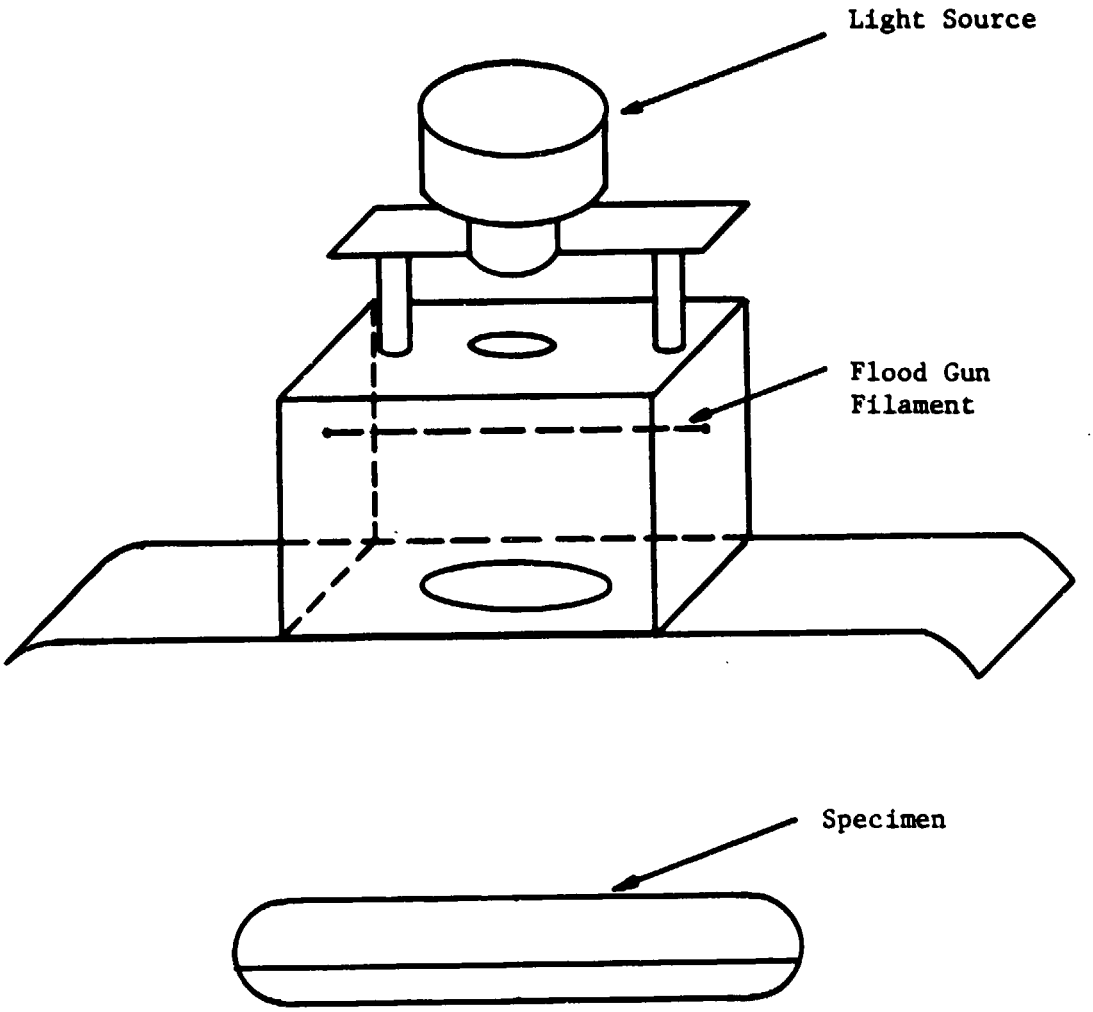

Figure 14. The light source installation.

The device was tested and a current of about 10^{-10} A was observed in the electrometer connected to the specimen. This meant that with a charge of about 10^{-7} C on the specimen, the discharge time would be about $T = 10^{3}$ s. This time period is quite slow compared to using the flood gun filament which takes only a few seconds. The reason for this slow discharging process could be because the light intensity was not high enough. A higher intensity device was not available and this method was abandoned.

The charging and discharging of the specimen was monitored by electrometers connected to the backside of the specimen. There was always a possibility that either some negative charges would remain on the specimen or that it would become positively charged.

H. Faraday Cup

The Faraday Cup was a collector cup which measured the beam strength. It was constructed from a light-weight stainless steel and it is shown in Figure 15. The cup was installed on the cylinder such that it straddled the slot as shown in Figure 16. It's seen that the beam can get into the cup easily. The cup was built such that the edges were bent toward the inside so there would be less chance for secondaries to escape from the cup. Furthermore, the inside of the cup was blackened with carbon in order to reduce the secondary coefficient of the primary electrons entering the cup(20).

To measure the beam strength, the cylinder was rotated until the cup was almost in the way of the beam and then, the beam was pulsed into the cup. When beam strength was not being measured, the cylinder was rotated so that the beam could enter the cylinder. The best

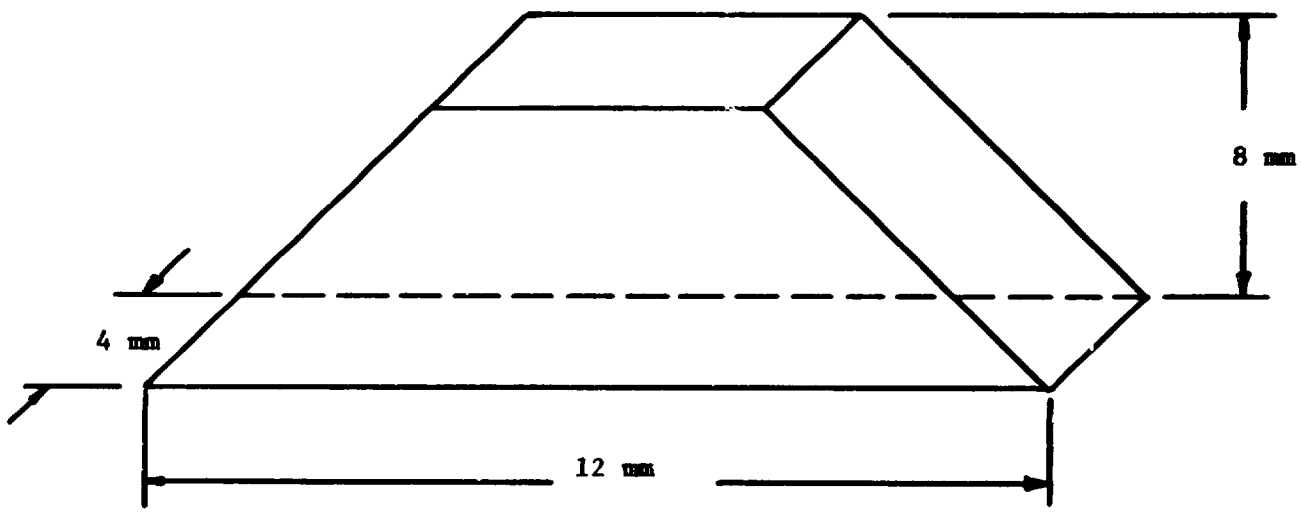

Figure 15. The Faraday Cup.

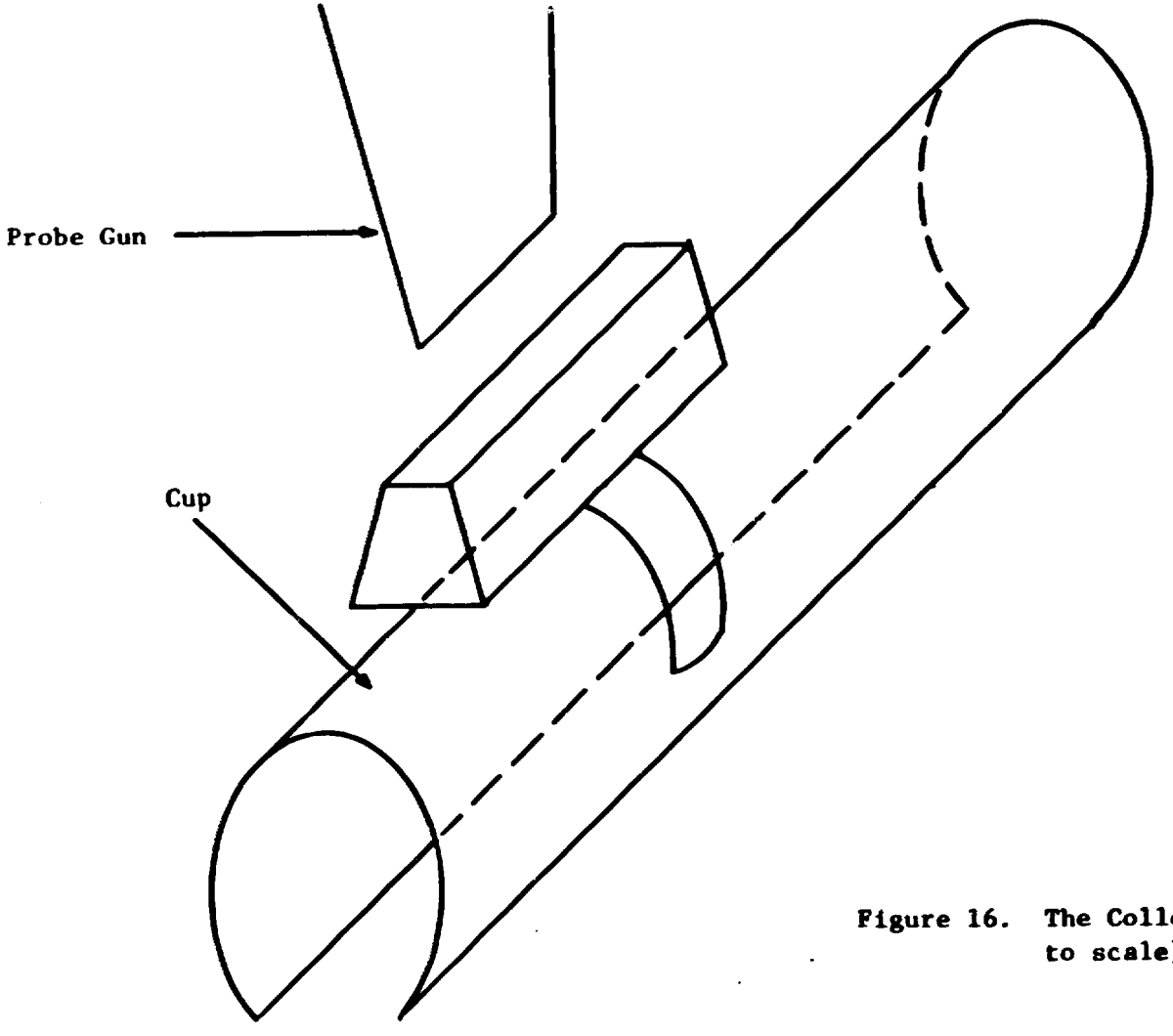

Figure 16. The Collector Cup (not drawn to scale).

advantage of this feature was that the cup was located outside of the electrostatic environment of the specimen; therefore, there was not any field perturbation. Also, it was easy to install the cup. The cup was tested by measurements explained in Chapter IV and it worked correctly. In the beginning another design for the Faraday Cup was considered. This design is explained here.

Next to the specimen, there was an opening which had a 1 mm width and a 10 mm length. Beneath the opening was a cavity in the platform as shown in Figure 17. The cup had the same form and was built from the same material as the last case. The cup was carefully inserted into the hole so that it didn't touch the grounded platform. The metal strip that supported the cup was insulated from the platform at connection points. A wire connected the back side of the cup to a pin outside the vacuum system for monitoring purposes. The beam was deflected into the cup so that its strength could be measured.

Note that installing this cup was very time consuming because the platform had to be taken out and a hole had to be made inside it. Inspite of time and effort that was put into this design, it didn't collect the beam completely. This was found out by doing secondary measurements for an uncharged specimen which will be explained in Chapter VI. Therefore, the other design was used and the results were satisfactory.

I. Noise

At times, electrical noise would cause the electrometer and the strip chart recorder to have a violent movement and oscillation. According to Budd(8), the noise was responsible for a ± 10% error in

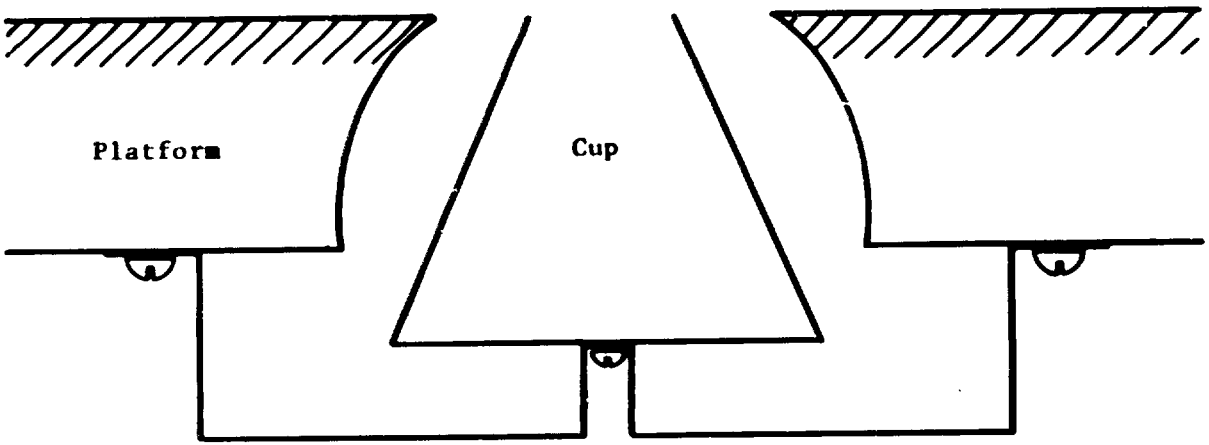

Figure 17. The first Cup design that didn't work.

his measurements. A careful study of the noise enabled the author to recognize the nature of the noise. The interesting result was that the nature of the noise was mechanical and not electrical.

The noise was displayed on an oscilloscope and it was found to contain two specific frequencies. One was a 40-60 Hz signal which was not very significant and the other was about a 300 Hz signal which came from a turbomolecular pump turning at 16000 rpm. The pump would cause vibration in the wires connected to the specimen and this was responsible for the noise observed with the electrometer. When the pump was turned off, the noise disappeared. Also, the vibration was excited by hitting the chamber with a hammer. The effect was a simultaneous increase in the noise level.

Besides responding to noise, the electrometer also drifted. Most of the time, the drift was a ramp caused by stray current; however, at times, the drift was observed to change spontaneously as well as in response to a change in operating conditions.

Since the cup was installed outside the cylinder, it was exposed to free electrons inside the chamber. As a result, a high drift rate was observed on the electrometer connected to the cup. Furthermore, sometimes a drift signal was observed on the specimen after it was charged. These drifts would make it hard to recognize the beginning or the end of the charge or discharge pulse on the strip chart recorder. An example of this situation and the noise is shown in Figure 18.

At some point, it was decided to bias the metal bell jar of the vacuum system to some positive potential so that scattered electrons

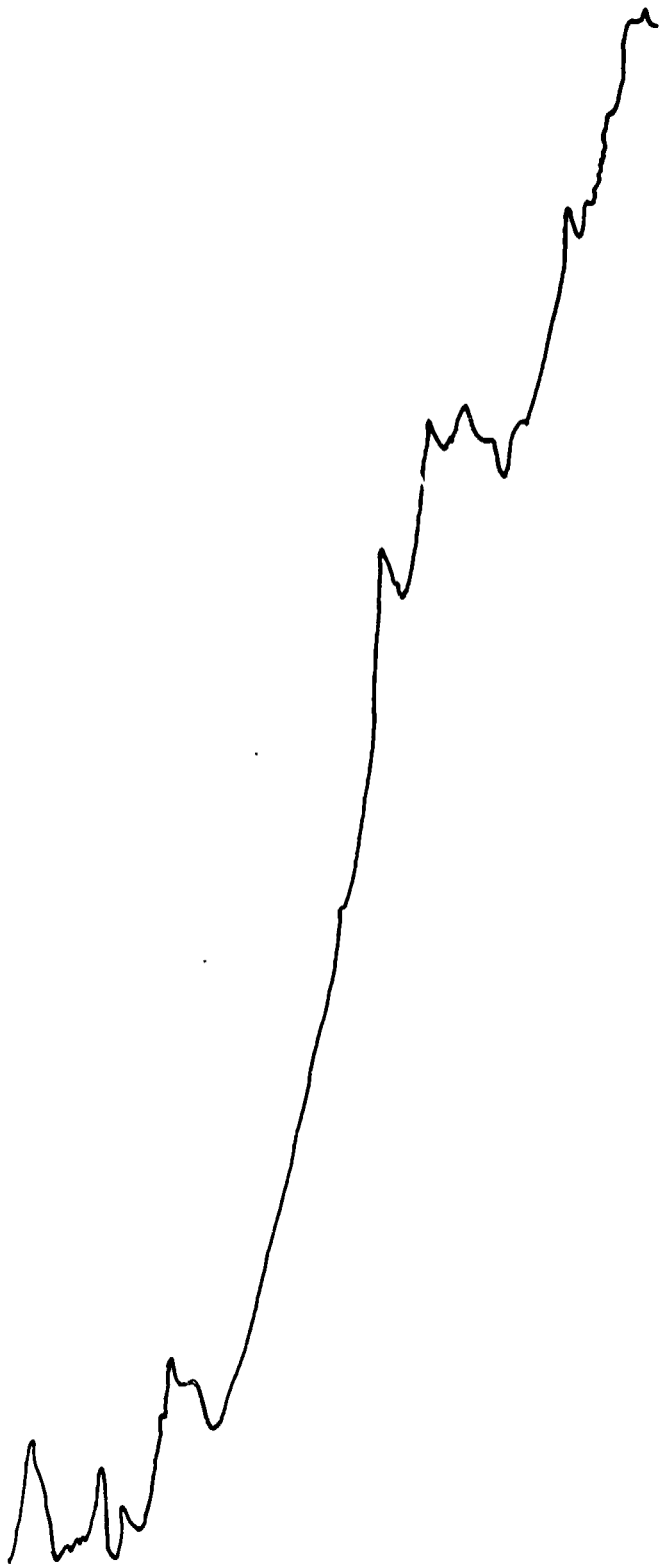

Figure 18. Noise added to the pulse.

which caused the drift would be absorbed by the jar and the drift would be reduced. Therefore, the platform was isolated electrically from the jar by using Teflon tapes and the jar was biased which caused the drift rate to change. It was not possible to isolate the jar and the platform permanently because of the special geometry of the jar, and this method was abandoned. However, the idea is very unique and it can be used for future designs.

J. Signal Monitoring System and Filters

Charge or currents that had to be measured were passed through a low pass filter and then they were monitored by a 600 B Keithley electrometer. The output of the electrometer was passed through another low pass filter and finally, the filter's response was applied to a strip chart recorder. This is shown in Figure 19. The first low pass filter (LPF1) had a major impact in reducing the noise level. This was because the noise was filtered out before it reached the amplifier in the electrometer.

Since the work dealt with currents on the order of picoamperes, the electrometer was set for a sensitive scale which was unstable in the presence of a filter with high capacitance. High value capacitors would turn the electrometer into a differentiator and as a result it was very sensitive to varying signals.

An RC low pass filter was designed with a 50MΩ resistor and the capacitance of a 60 cm long transmission line (42 PF). Figure 20 shows the filter and other features of the electrometer circuit. At times, when more filtering was desired, extra capacitance was added to the filter. Since the electrometer had an OP-amp with feed back,

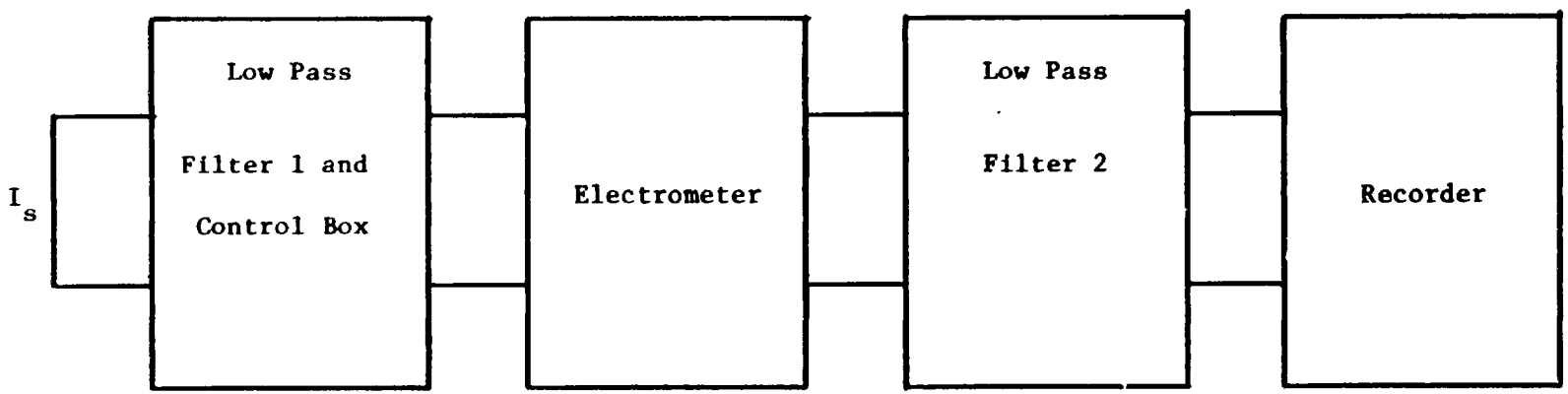

Figure 19. The monitoring devices.

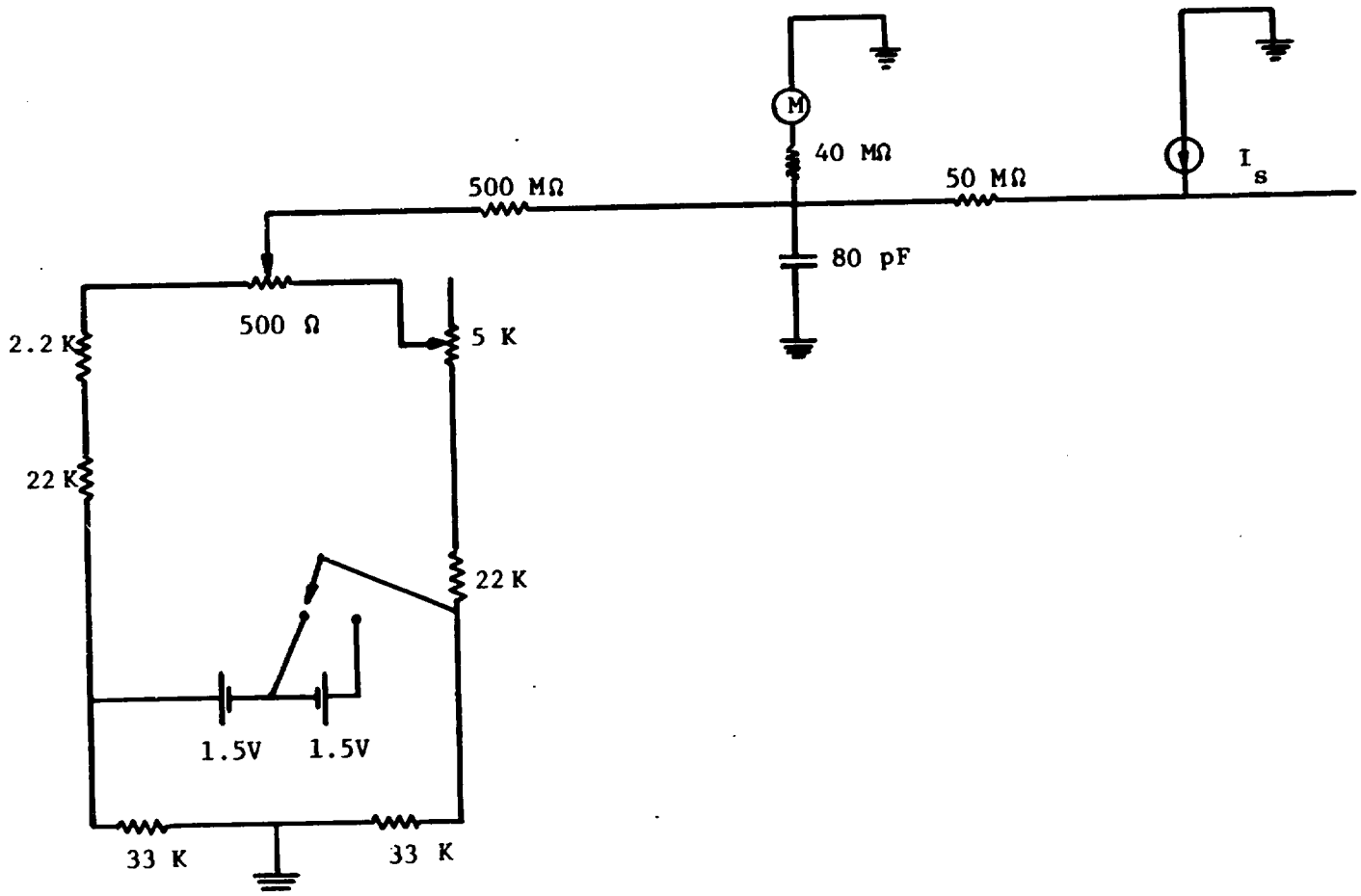

Figure 20. LPF1 and control box.

its input resistance was practically zero. As a result, the filter's capacitor was practically shorted; therefore, a 40MΩ resistor was put in series with the electrometer to provide a higher value of load impedance in parallel with the capacitor.

A biasing circuit produced a D.C. current which cancelled the drift produced by either the specimen or the cup. The amplitude of the D.C. current was controlled by adjusting a pot. This device was electrically connected to the low pass filter LPF1 and it is also shown in Figure 20.

III. MATHEMATICAL MODELING OF THE SYSTEM

Mathematical modeling of the surface potential is explained in detail in previous works(6,7); however, a brief review of these models and assumptions is necessary.

Three-dimensional simulations have shown that the system can be modelled in two dimensions with some associated error which is small for the experimental geometry. If the cylinder length is 2.5 times the diameter and if the specimen length is equal to the cylinder diameter, then the error in two dimensional calculations is negligible (3). This was shown by finding the solutions of Laplace's equation in terms of orthonormal functions(19). Two dimensional simulation has made the computation of potential and fields simpler. It uses a conformal mapping which transforms the half cylinder represented by a semicircle, into a plane as shown in Figure 21. The semi circle has radius a and the specimen width is 2B, as shown in Figure 21. Points inside the semicircle (W - plane or U + iv) are transformed into the Z plane (or x + iy) by the mapping

$$Z = \frac{2W}{1 + (W/a)^2} \tag{41}$$

which cuts the circle at W = ia and opens it into the Z plane. The three points -a, 0, a along the V axis don't move. However, the edges of the specimen at $W = \pm B_s$ transform into new positions at $Z = \pm B$. Since the specimen width B_s is small compared to a, the transformed specimen width is approximately twice the original one.

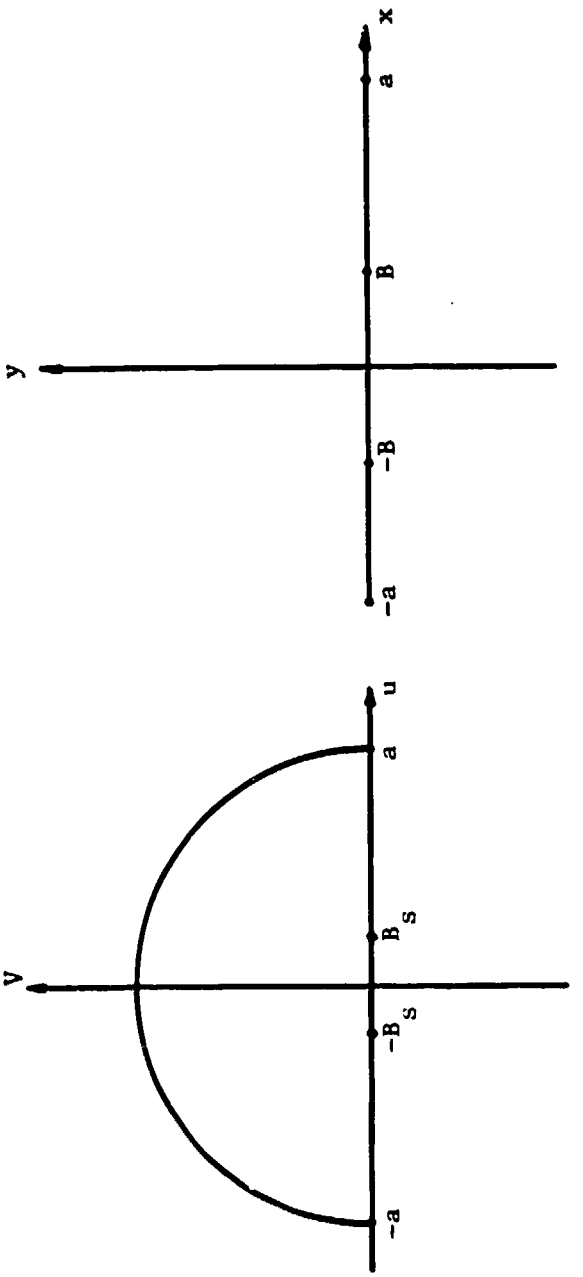

Figure 21. Geometry of the conformal mapping.

The potential of a point is the same in both the W plane and the Z plane; however, the field components are different and they have to be transformed back to the original (or W) plane. Therefore, it is necessary to find the derivative of the transformation $\frac{dZ}{dW}$ (or s + it) which is given by

$$\frac{dZ}{dW} = \frac{2\{1 - (W/a)^2\}}{\{1 + (W/a)^2\}^2} \quad . \tag{42}$$

Once s and t are obtained, the inverse transformation of the field components is done by using(1)

$$E_u = s\,E_x + tE_y \tag{43}$$

$$E_v = -tE_x + sE_y \quad . \tag{44}$$

The surface potential V(x) is defined to be a polynomial in the transformed variable and it is given by

$$V(x) = \sum_{n=0}^{N} A_n (x/B)^n, \text{ N finite} \tag{45}$$

It has been assumed that the potential has even symmetry about the origin with even n's. The potential of a point (x,y) in the Z plane is given by

$$V'(x,y) = \frac{y}{\pi} \int_{-B}^{B} \frac{V(\eta)\, d\eta}{(x-\eta)^2 + y^2} \tag{46}$$

where the integral is taken over the specimen's surface.

A. Measuring the Surface Potential

At the center of the specimen fields are normal. This can be shown by considering the shape of the potential curve as shown in Figure 22 and the relationship $E = -\nabla V$.

If the beam is normal to the specimen and no deflection voltage is applied, it will hit the center of specimen. This is due to the fact that, at the center, fields are normal and they will not bend the beam. This allows us to measure the surface potential with direct beam impact in the center of the specimen.

The surface potential V_0 is less than the high voltage bias on the flood gun because the surface charge stabilizes at an equilibrium state where there is a unity secondary coefficient. At this point, for any electron that strikes the specimen one leaves. Any particle with energy larger from this equilibrium energy can either charge or discharge the specimen.

To measure the surface potential experimentally one first charges the specimen by rotating the platform to a position where it is normal to flood gun and turning the flood gun on. Then the platform is rotated to the position of normal incidence for the probing beam and the cylinder is rotated to allow the beam to strike the specimen. The high voltage of the pulse circuit (or V_{high}) is set such that the beam is hitting the platform and not the specimen. The low voltage (or V_{low}) is set such that the beam will hit the center of the specimen when the pulse is triggered. The metal coating behind the center of the specimen is connected to an electrometer which monitors the charging or discharging of the surface. Then the probe beam voltage

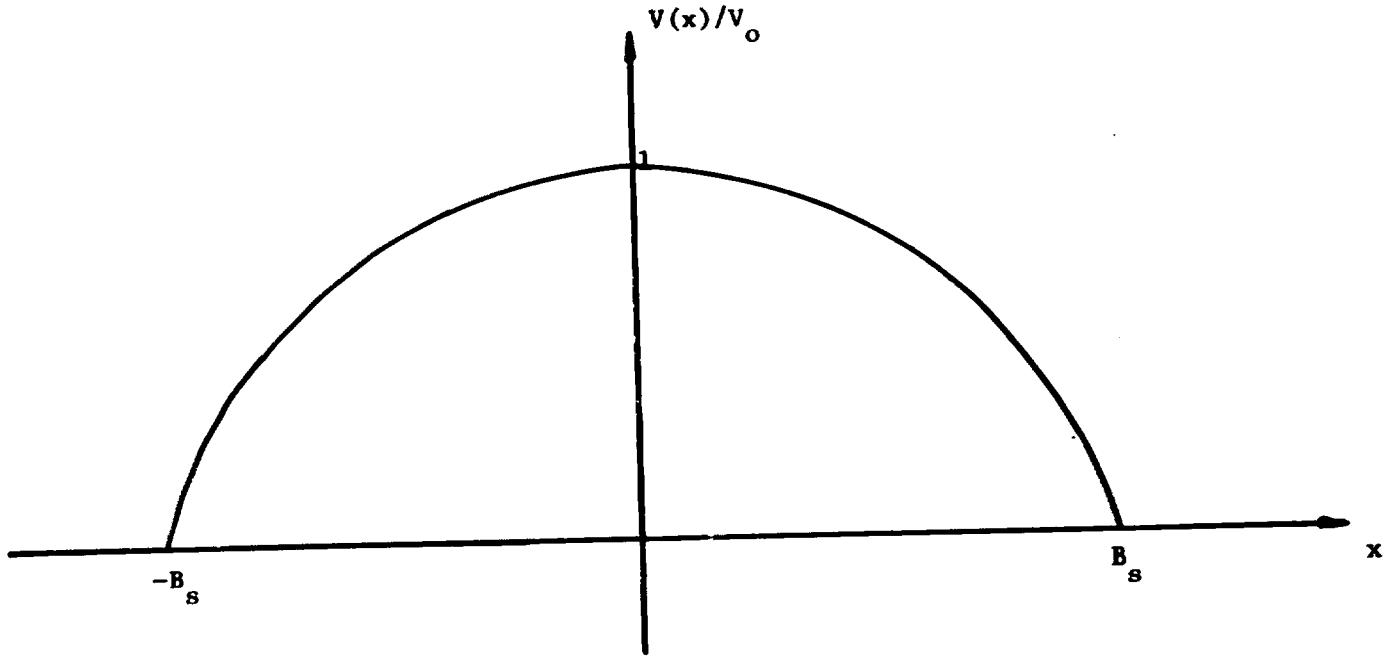

Figure 22. The normalized potential distribution on the surface of the specimen.

is set at a value less than the surface potential V_0 so that the beam will not hit the center of the specimen.

At this point, a pulse is triggered. After each trigger, the beam voltage is increased by steps of 50V until a response occurs. The first voltage that causes a response is the surface potential.

When the beam hits the specimen the surface potential will change due to charge or discharge of the surface. After this happens, the cylinder and the platform have to be rotated to the charging positions and the specimen has to be recharged. The electrometer indicates whether or not the specimen is struck and its response is shown qualitatively in Figure 23. The small negative portion of the curve is seldom seen and corresponds to the region for which δ is less than one.

Table 1 shows the surface potential measured for different flood gun voltages. The first entry(12, 10.1) was measured a few months before the second entry (12.6, 10.2) was measured. As we see, the difference (12-10.1) is not equal to the difference (12.6-10.2). This is due to the fact that the characteristics of the specimen had changed. Possible reasons for this change are contamination of the surface and use. A difference of 2.7 kV was measured in previous work(8). The difference between 12.6 and 10.2 is 2.4 kV which is very close to the value of critical energy used for calculation of secondary coefficient in Chapter IV.

B. Particle Trajectories (non-impacting)

Particle trajectories are found experimentally by using detector wires on the cylinder. These deflection measurements are done by

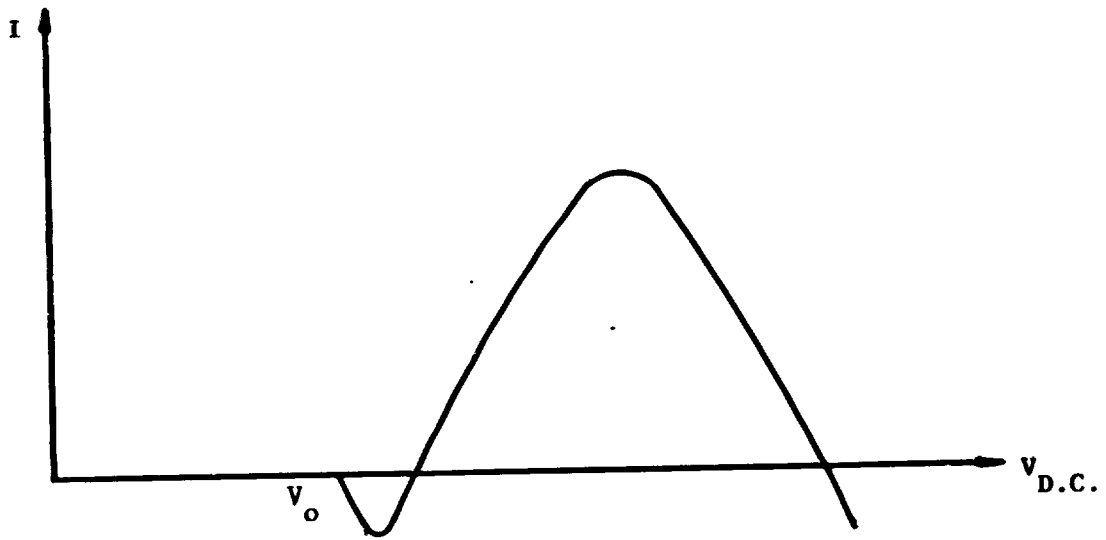

Figure 23. Illustration of the electrometer's response vs. the beam's voltage when surface potential is being measured.

Table 1

SURFACE POTENTIAL AT THE CENTER FOR DIFFERENT FLOOD GUN VOLTAGES

Flood Gun Voltage (kV)	Surface Potential (kV)
12	10.1
12.6	10.2
10	8.1

charging the specimen first. This is done by rotating the cylinder and the platform to the horizontal position and turning on the flood gun system. Then the probe beam is turned on with a bias less than the surface potential so it can't hit the specimen. One of the detector wires is connected to an electrometer and the other electrometer is connected to the backside of the specimen. This second electrometer shouldn't indicate any response; otherwise, it means that the surface of the specimen has been struck and the specimen has to be recharged. The platform is set at a desired position and a power supply is connected directly to the deflection plates. This voltage is varied until a response is observed in the detector wire. If no response is observed then the cylinder position is changed and the voltage is varied again.

Figure 9 shows how the beam is deflected. In this figure the source point of the electrons is assumed to be 1 cm from the cylinder. However, the source point used by the simulation is the point where the trajectory first crosses the cylinder. The angle of incidence θ_{in} was found from

$$\theta_{in} = 90° - (Pl_r - Pl_p) \times 1.8° \tag{47}$$

where Pl_r is the platform position for which the incident beam is normal to the specimen. This corresponds to a platform position of 25 because the platform position 00 is horizontal and the probe gun is set approximately at a 45° angle with respect to the horizontal plane. Due to slight misalignment in the system, a platform position of 27 was a better choice for normal position. This was verified using deflection measurements and secondary coefficient measurements as will be shown in Chapter IV. The exit angle θ_{out} is obtained from

$$\theta_{out} = (Cyl_p - Cyl_r) \times 1.8° + \theta_{in} \tag{48}$$

where Cyl_p is the cylinder position and Cyl_r is the cylinder position for which the beam hits a detector wire directly before entering the cylinder.

An experiment was conducted to measure Cyl_r using a 9.5 kV probe beam with a detector wire connected to an electrometer. The cylinder was rotated and the deflection voltage was changed until the beam could hit the wire directly. The results are shown in Table 2. The first column is the cylinder position, the second column is the deflection voltage and the third column is the current in the detector which is much larger for a direct hit than when a reflected beam hits the detector wire. From data in Table 2, the cylinder position that corresponds to correction deflection voltage V_D was found to be 73.7. Therefore, the equation for exit angle θ_{out} becomes

$$\theta_{out} = (Cyl_p - 73.7) \times 1.8° + \theta_{in} . \tag{49}$$

The reference platform position was chosen to be 27 because it provided the closest match between the simulated exit angle and experimental exit angle. The angle of incidence θ_{in} was found by using Equation 50

$$\theta_{in} = 90 - (27 - Pl_p) \times 1.8° \tag{50}$$

where Pl_p is the platform position.

The summary of equations used to find particle trajectories are as follows.

Table 2

CYLINDER POSITION, DEFLECTION VOLTAGE AND CURRENT IN THE DETECTOR WIRE FOR A SAMPLE DEFLECTION MEASUREMENT

Cylinder Position	Deflection Voltage	I (A)
75	360	$.7 \times 10^{-9}$
74	+39	$.7 \times 10^{-9}$
73	-343	$.7 \times 10^{-9}$

$$\phi = 1.67 \times 10^{-4} \left(\frac{9.5}{E} V_{Def} + V_D\right)$$

$$\phi = -1.4\phi$$

$$\theta'_{in} = \theta_{in} + .4\phi$$

$$\theta_{in} = [90 - (27 - Pl_p) \times 1.8°] \frac{\pi}{180}$$

$$\theta_{out} = (Cyl_p - 73.7) \frac{\pi}{100} + \theta_{in} \qquad (51)$$

The first three of these equations were developed in Chapter II, where the deflection factor D was explained. The parameters, V_D and Pl_r, assigned the value of 27, were determined as explained in the next section.

C. Determination of V_D and Pl_r

This section shows how parameters V_D and Pl_r are determined by simulation. Parameters necessary to determine particle trajectories are the coefficients of the potential polynomial, the degree of the polynomial, cylinder radius, the specimen's width, energy of the probing beam, corrected angle of incidence ϕ (Figure 9) and corrected input angle θ'_{in} for the incident beam. The exit angle θ_{out} was found experimentally by detector wires as explained in the earlier parts. This measured value was compared to the simulated value for different values of V_D and Pl_r so that optimum values could be found. A few samples will show how these parameters are obtained.

A deflection measurement was done for a surface potential of 10 kV, a probe beam voltage of 9.5 kV, and a platform position 25,

such that the beam was nearly normal to the surface. Values of deflection voltage and cylinder position for which the deflected beam hit the wire were obtained. Based on these values simulations were done for a potential distribution of degree 4 or N = 4 and for V_D = 70 V. Therefore, the equations necessary to calculate ϕ, ϕ', θ' and θ_{out} can be found from Equation 51. The values of ϕ, ϕ' and θ' are used to calculate the exit angle θ_{out} by simulation. These values and the values of θ_{out} obtained by deflection measurements are shown in Figure 24. The abscissa is the angle ϕ in m rad.

Another experiment was done by holding the cylinder in a fixed position and varying the deflection voltage until the deflected beam hit the detector wire. Then the platform was rotated one step and the deflection voltage was varied until the beam hit the wire again. One of these experiments is explained in more detail here. The specimen is charged with a 12 -kV flood gun voltage. Then deflection measurements are done using a 5 -kV probe beam. Therefore, the deflection factor D is 3.17×10^{-4} rad/V. The cylinder position was set at 120 in the experiment and the cylinder reference position of 73.7 was used in the simulation. Also, N was set to be 4 and V_D was chosen to be 70 V in the simulation. Using the above parameters, ϕ, ϕ' and θ_{in} were calculated and computer simulations were done to obtain the exit angle θ_{out}. These values and the values of θ_{out} obtained by experiment are shown in Figure 25. The abscissa is the angle ϕ in m rad.

We close this section by providing the summary of parameters that we have used consistently through our work. A cylinder reference position Cyl_r of 73.7 and a platform reference position Pl_r of 27 were used. The reference deflection voltage was 70 and the deflection

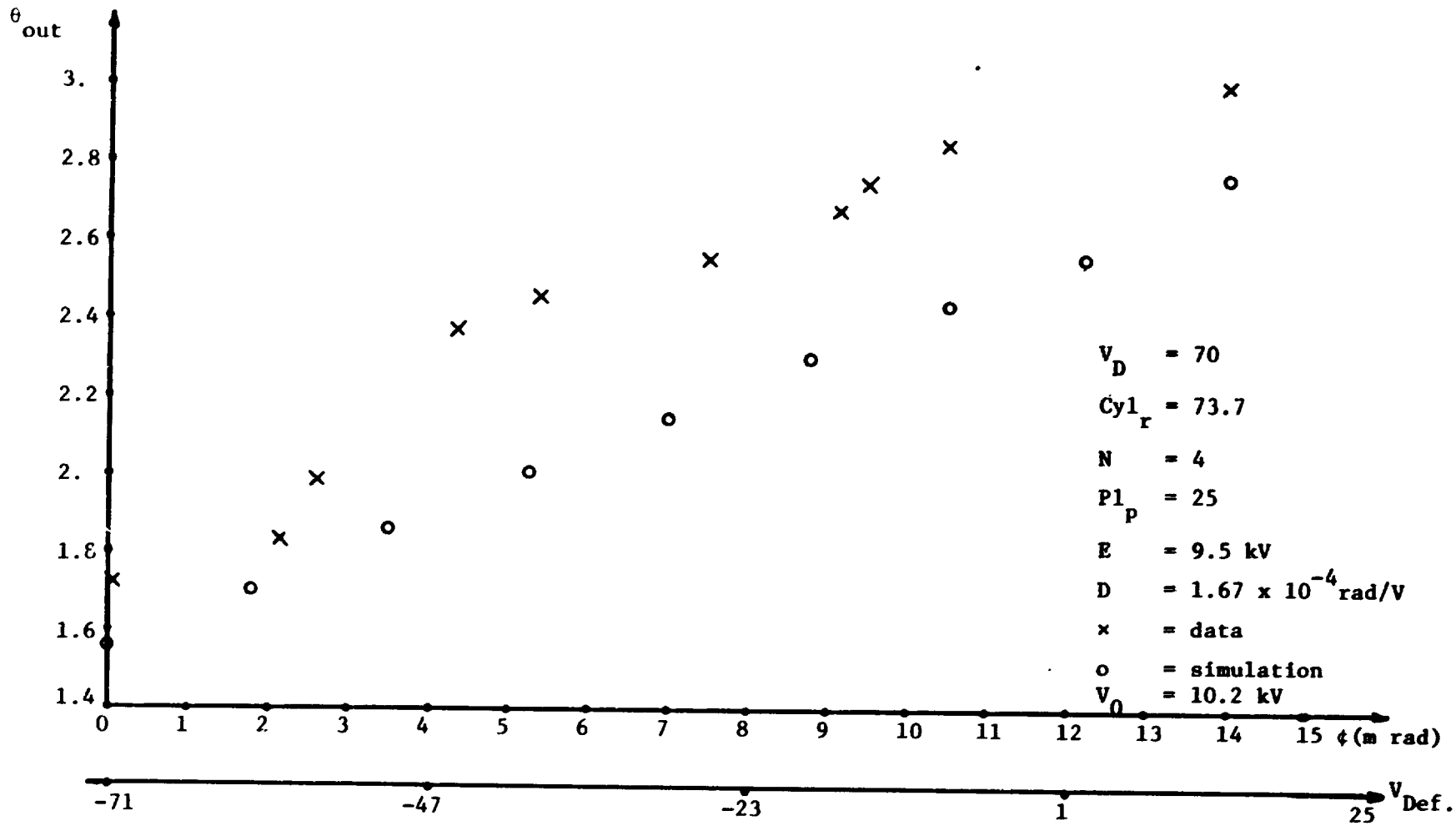

Figure 24. Plot of simulated and experimental exit angle for the case when the probe gun is centered above the specimen.

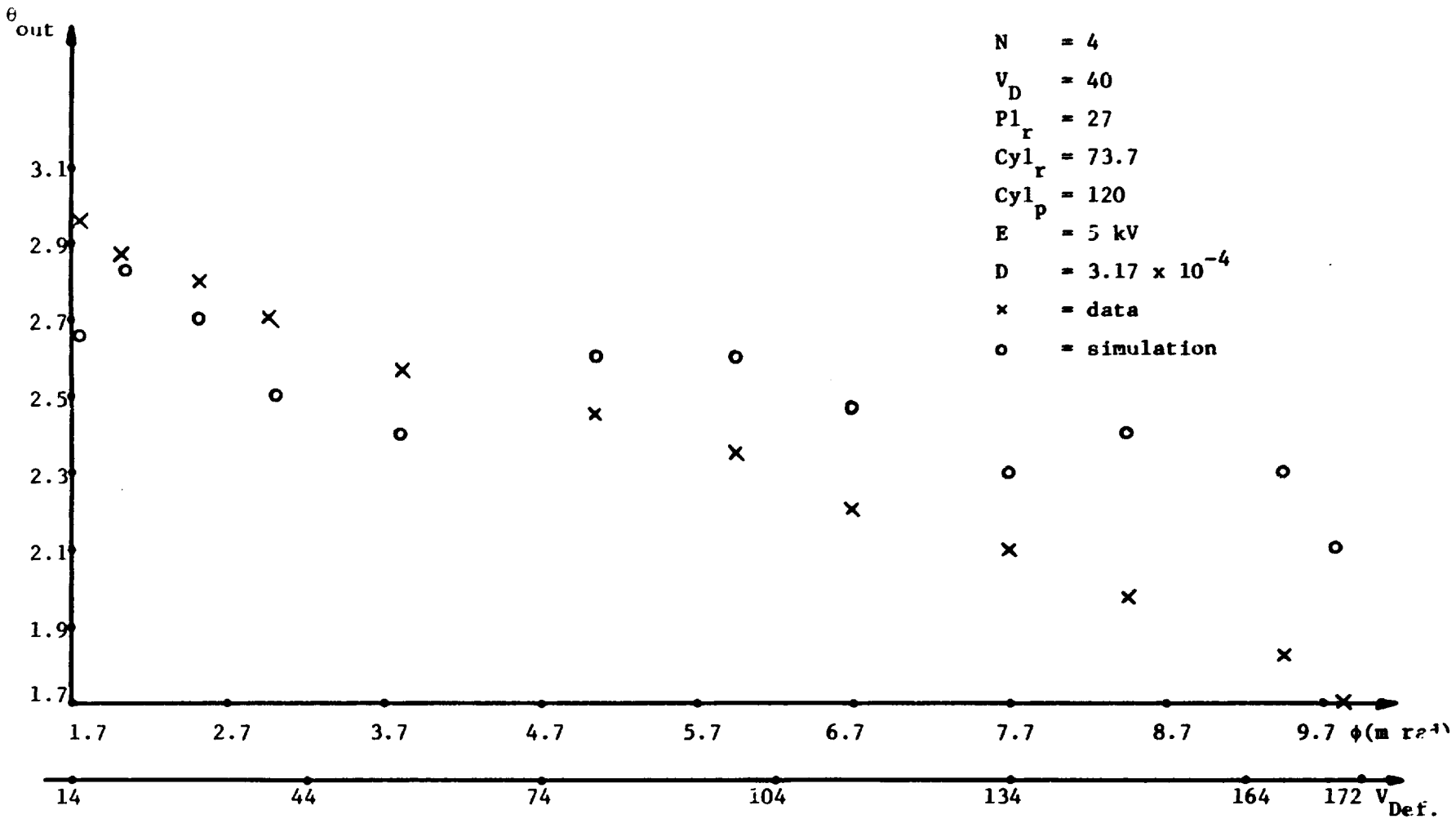

Figure 25. Plot of simulated and experimental exit angle for different platform positions.

factor D was of the form 1.67×10^{-4} $(\frac{9.5}{E})$, where E was the primary beam energy and 1.67×10^{-4} was the deflection factor for a 9.5 kV probe beam. The degree of the surface potential polynomial N was set at 4.

IV. SECONDARY EMISSION MEASUREMENTS

The secondary emission coefficient was obtained in two ways, one using the experimental data and the second using the theory. The two values so obtained were tabulated and compared with each other.

The experimental data were taken by charging the specimen to 10.2 kV as explained in Chapter II. Measurements were done for normal and oblique incidence with different beam energies. For normal incidence the platform was set at position 27 and for oblique incidence, platform positions of 35, 50, 55, 60 and 65 were tested. The beam's charge was measured by the Faraday Cup at the end of each experiment. If more beam current was desired, the filament was turned higher and the experiment was repeated. The charge measurements were done using a 600B electrometer as explained in Chapter II.

The values of σ predicted by theory were obtained by using Equation 12 and Equation 29 in Chapter I. The impact energy and the angle of incidence were determined by computer simulations as explained in Chapter III. These values and the values of σ obtained by experiment were compared by drawing curves of σ vs. impact energy or impact point.

A. Calculation of Secondary Emission Coefficient

The measured secondary emission coefficient σ was obtained by using

$$\sigma = 1 - \frac{Q_s}{Q_c} \tag{52}$$

where Q_s is the charge released by the specimen and Q_c is the charge collected by the cup. Note that the beam's charge Q_c is negative. If the specimen releases electrons then the pulse recorded is positive, Q_s is positive, and σ is greater than unity. This corresponds to either

low impact energies or high impact angles. If the specimen accumulates electrons then the pulse recorded is negative, and Q_s is negative, and σ is less than unity. In this case the secondary coefficient corresponds to high impact energies.

The beam's charge Q_c is a function of the filament's current and the primary energy E. The pulse width was 28 ms; therefore, a charge Q_c of 10 PC could be produced by a beam current of

$$I = \frac{Q_c}{T} \approx 0.36 \text{ nA} \tag{53}$$

B. Procedure to Find σ

The experimental data was taken by the procedure explained here. The cylinder had to be set at 00 position with the opening facing the flood gun when the specimen was to be charged or discharged. These procedures are explained in Chapter II. Then the cylinder had to be rotated so that the opening was underneath the platform and the specimen was surrounded by the grounded metal surface of the cylinder. The slot allowed the beam to enter the cylinder, and the cup, which was mounted over the slot, had to be kept away from the beam. At the end of the experiment, the cylinder was rotated until the cup was almost in the way of the beam so that the beam could easily be deflected into the cup and measured. The platform position was first set at zero so that it faced the flood gun. After the specimen was charged, the platform was then set at a position desired for measurements.

The pulse-circuit bias V_{high} was set such that the beam could not hit the specimen and the low-voltage bias V_{low} was set depending on the

desired impact point. Sometimes, prior to the measurements, the filament was turned on and was left to stabilize to a certain point. Then when meansurements were to be made, the probe beam voltage was set to a desirable voltage. This voltage changed when the filament current changed because of the resistor which was in series with the voltage power supply. Therefore, the beam voltage had to be checked frequently and adjusted as necessary. The electrometer was set to the least sensitive scale (10 μc) during the charging or discharging process and it was set to the most sensitive scale (1 pc) when the pulsed beam was used. The strip chart recorder was calibrated so that its full scale deflection corresponded to that of the electrometer. Before any measurements with the sensitive scale, the electrometer's needle was released and the drift current was neutralized by using the D.C. bias box explained in Chapter II.

A summary of the procedure is listed below.

1. Turn on the beam filament, set V_{high} of the pulse circuit and calibrate the strip chart recorder.
2. Charge up the specimen with platform position set at 00.
3. Rotate cylinder and platform to proper positions.
4. Set beam voltage and V_{low} of the pulse circuit.
5. Release the electrometer's needle, neutralize the drift current, turn the recorder on and trigger a pulse.
6. Rotate the cylinder to the proper position, set V_{low} to the proper value, trigger a pulse and measure the beam's charge Q_c.

Anytime the specimen is struck by the beam, its surface potential changes; therefore, the data taken after several impacts is not reliable because the potential distribution is distorted. Thus, only a few data

points were taken at different spots on the specimen which was then recharged before additional measurements were made.

C. Measurement of σ for Normal Incidence (uncharged specimen)

The main purpose of this measurement was to make sure that the cup was working correctly. This was done by comparing the value of charge deposited on the surface of the specimen with the one measured by the cup.

To do measurements with an uncharged specimen, it had to be discharged first. This was done as explained in Chapter II. Then the cylinder was rotated until the opening was under the platform. The platform was set at normal position which is 27 and the high voltage of the pulse circuit was selected. As explained in Chapter III, the right choice of deflection voltage would force the beam to hit near the center of the specimen. The secondary coefficient σ was measured for different points of the specimen's surface to observe the variation of σ near the center. These values were approximately the same because the beam was normal to the surface. Since the specimen was discharged, the impact energy was the energy of the beam. Therefore, the values of σ obtained for this relatively high energy could be compared to the theoretical value of σ for high impact energies and normal incidence. The theoretical value of σ is calculated by using Equation 12. For an uncharged specimen, the value E_c was 1.5 kV and the exponent n was 0.6(8). Figure 26 shows the values of σ obtained by the experiment and the values of σ calculated according to Equation 12. This graph is a firm indication that the values measured in this work correspond to Budd's work(8) and that the Faraday Cup installed on the cylinder measures the correct value of the beam's charge.

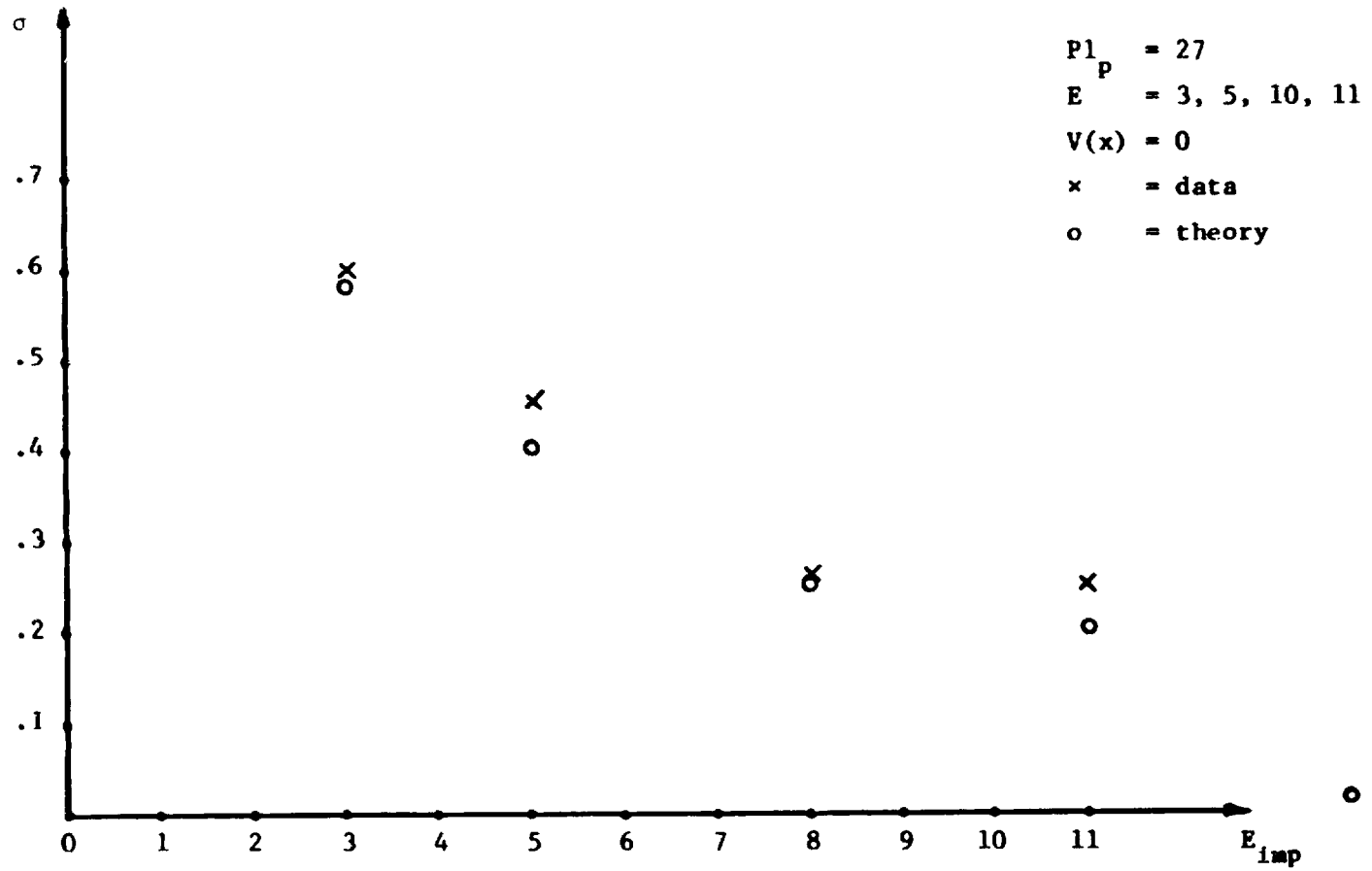

Figure 26. Plot of σ for normal incidence with an uncharged specimen.

D. Measurement of σ for Normal Incidence (charged specimen)

The main purpose of this series of measurements was to show that for platform position 27, the platform was normal to the beam. This was done by observing whether or not σ was a symmetric function of the beam's deflection voltage V_{low}. This platform position was defined in Chapter III and it was called the platform reference position Pl_r. The value of deflection voltage which corresponds to the center of the symmetric curve was defined in Chapter III and it was called the correction deflection voltage V_D. Another purpose was to find parameters E_c and n in Equation 12 so they can be used later in oblique incidence measurements.

This series of measurements was similar to the one for the uncharged specimen; however, the specimen had to be charged first. The cylinder and the platform were set to 00 position and a 12.6 kV flood gun beam was used to produce a 10.2 -kV central surface potential on the specimen. Then the cylinder was rotated until the opening was beneath the platform and the platform was set at or near 27 which is normal to the gun. The probe beam was turned on and secondary measurements were done for different energies.

One of these measurements was the case for an 11 kV beam energy. Figure 27 shows σ for platform positions of 25, 27 and 30. The abscissa is the deflection voltage; the first point and the last point are the edges of the specimen. As it is seen the case for the platform position of 27 is the most symmetric. This means that in this platform position, the beam impacts near the center of the specimen with a normal angle of incidence. The beam doesn't impact the specimen at a right angle for the platform position of 25 and 30. As a result σ is less symmetric with

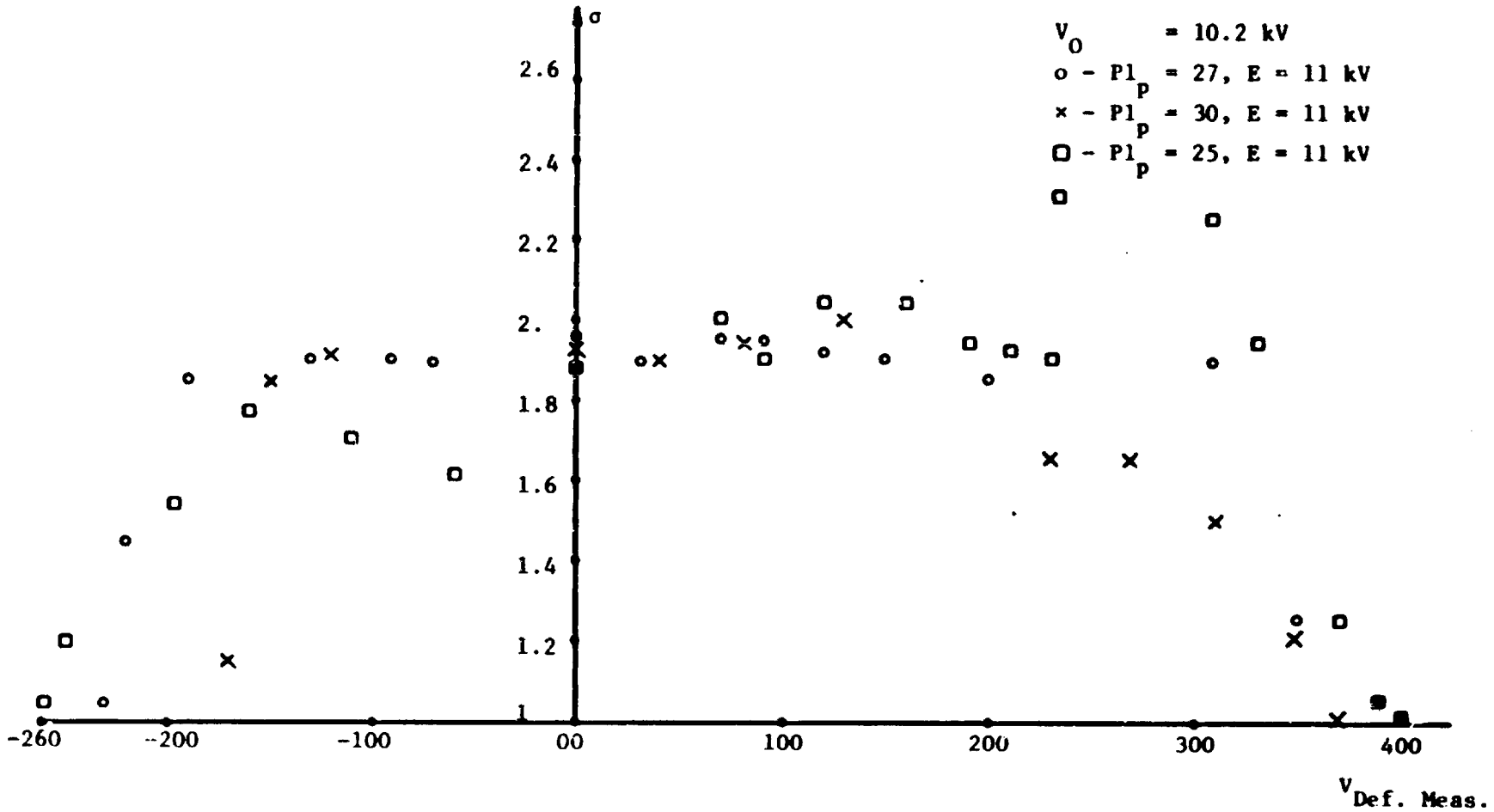

Figure 27. Plot of σ vs. deflection voltage different platform positions and 11-kV beam energy.

respect to deflection voltage.

As it is seen, the curve of σ vs. deflection voltage for the case of platform position at 27 is centered around a deflection voltage of about 80 volts and not zero. This offset is due to slight misalignment caused by replacing the filament as explained earlier. The important feature of this curve is the confirmation of the value 27 for the platform reference position Pl_r. Also, the value of exponent n in Equation 12 was found from these data and data taken from similar experiments with beam energies of 12, 13 and 14 kV to be 0.8. The value of exponent n depends on the type of material used and it can be determined by fitting Equation 12 to the experimental data.

The critical energy was found by using Table 1. The center surface potential for a 12.6 kV flood gun beam was 10.2 kV. The difference between these two numbers which was 2.4 kV was the critical energy for a 10.2 kV surface potential. However, the critical energy for a discharged specimen was about 1.5 kV. A high current beam was used to bombard the specimen in that voltage range near the critical point where there was little response observed on the electrometer.

E. Asymmetric Potential Distribution

Though the work reported here is for a specimen with a symmetric potential distribution, the test described in this section is for an asymmetric potential distribution. The symmetric distribution occurs when charged particles emitted from the flood gun filament hit the surface of the specimen at a normal angle of incidence. However when the specimen is tilted during the charging, an asymmetric distribution occurs.

One experiment was done with a non-symmetric potential distribution on the surface. The platform was tilted 5 steps (9°) from the 00 position and then a 12.6 kV flood gun voltage was used to charge the specimen. Figure 28 shows how particles impact the surface of specimen in this case. Then the platform was set at 27 and normal incidence measurements were done with an 11 kV beam energy. Note that in this measurement everything was similar to the case for normal incidence measurements except that the platform was tilted during the charging process.

The secondary coefficient σ is shown in Figure 29 and contrasted to the data taken from the symmetric case shown in Figure 27. The curve of σ vs. deflection voltage is not symmetric because the potential on the surface is not symmetric. This curve suggests that the potential distribution on the surface of the specimen is relatively high on one side resulting in high secondaries and low on the other side resulting in low secondaries.

F. Calculation of σ Predicted by Theory and Curves of Measured Data Vs. Impact Energy

The basic Equation 29 used to calculate σ from theory was expressed in Chapter I and is repeated here for convenience:

$$\sigma_{th} = \left(\frac{E_c}{E_{imp}}\right)^n \frac{1}{\cos\theta'} \qquad (29)$$

The critical energy E_c and the exponent n are defined in the previous section. The angle θ' is defined to be the angle of the impacting beam from the normal to the surface of the specimen. This can be obtained as shown in Equation 54.

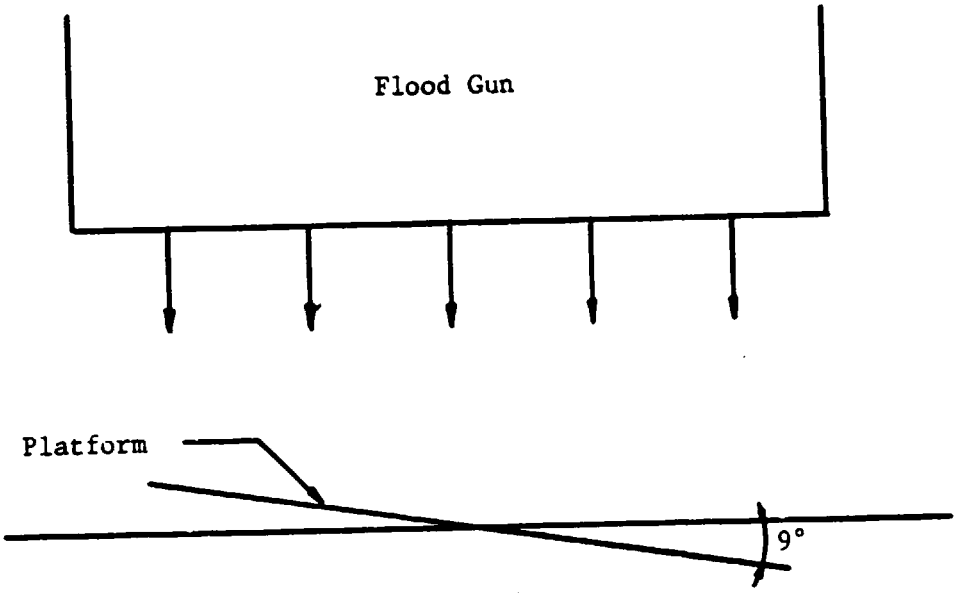

Figure 28. Platform tilted to achieve asymmetric potential distribution.

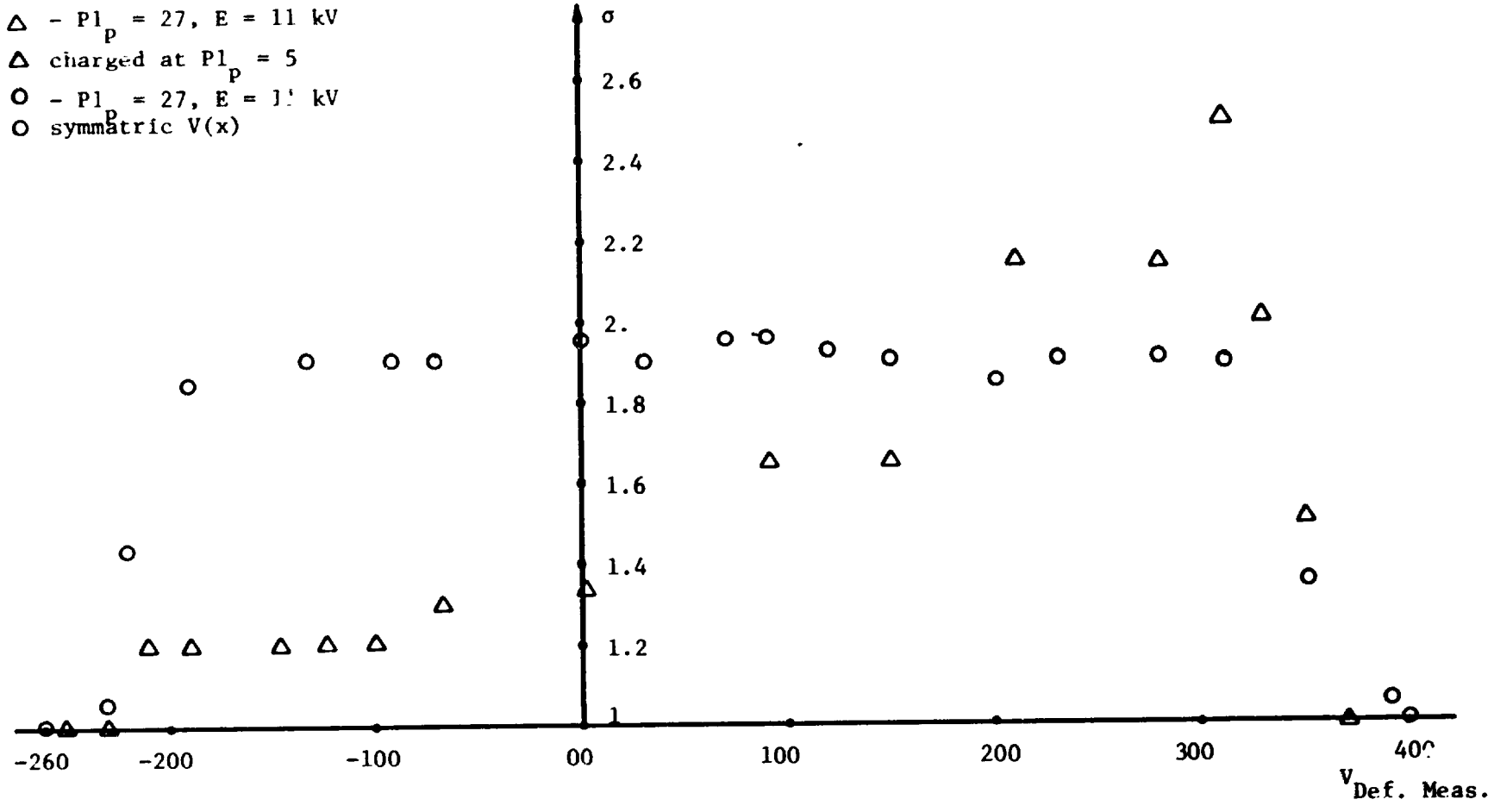

Figure 29. Plots of σ for two cases of symmetric and asymmetric potential distribution.

$$\theta' = 90 - \theta_{imp} \tag{54}$$

where θ_{imp} is the impact angle shown in Figure 30. This angle is the inverse tangent of the ratio of the velocity in the y direction to the one in x direction, as shown by

$$\theta_{imp} = \tan^{-1} \frac{V_y}{V_x} \quad . \tag{55}$$

Velocities V_y and V_x are obtained from the computer simulations.

Once θ' is determined, σ_{th} can be calculated independently from the experimental data and the two values can be compared with each other. This comparison was done for different platform positions and beam energies. Each set of experimental data was taken for a specific surface potential, platform position, and beam energy. Then computer simulations were done for each specific case to find the potential on the surface of specimen V(x), impact angles θ_{imp}, and the impact points x.

Two special points were identified. The first point was the edge of the specimen and the last point was either the second edge or the point that the beam couldn't hit the specimen anymore. The range of deflection voltages was determined by these two points and it was the same for both simulation and experiment. However, the deflection voltages corresponding to the two points were different for simulation and experiment. The range of deflection voltage R' is defined as

$$R' = V_2 - V_1 \tag{56}$$

where V_2 is the deflection voltage for which one edge of the specimen is detected and V_1 is the deflection voltage for which either the other

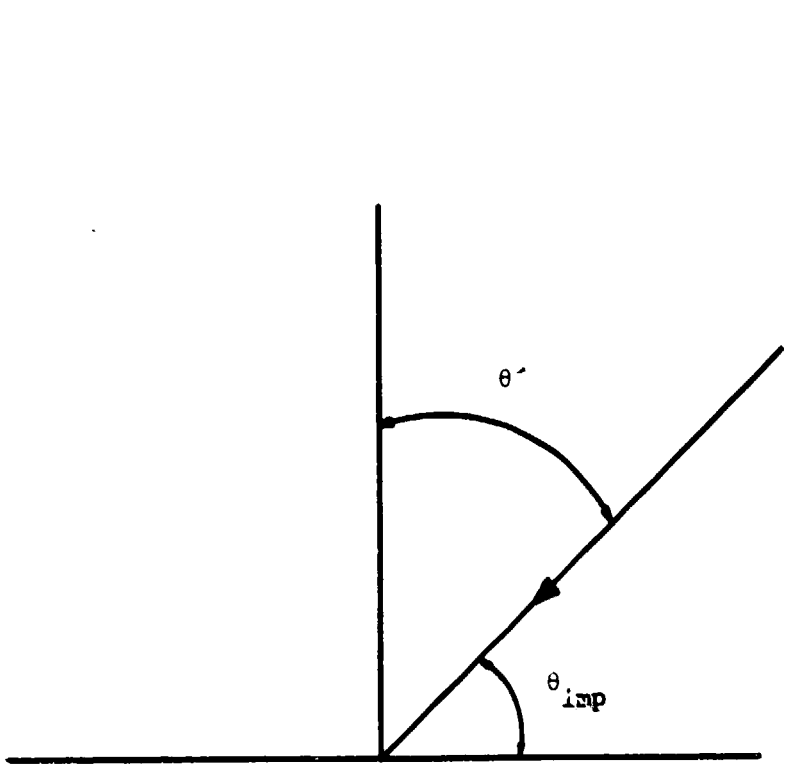

Figure 30. Geometry used to calculate angle θ´.

edge is detected or the beam no longer strikes the specimen. The beam is lost when the platform is tilted from the normal position and the particles approach the specimen with low impact angles or high x-directed velocities.

Figure 31 shows plots of V_1 and V_2 vs. platform position for a 9 kV beam and surface potential of 10.2 kV. The values obtained from the simulation are shown by circle's and those obtained by measurement are shown by x's. The subscript (1) indicates the value for which the edge is detected and subscript (2) shows the value for which the beam is lost.

The value of R obtained from the experimental data had to be matched to the one obtained from the simulation. To do this, high current beams were used to detect the edges of specimen or the point that the beam was lost. In almost every case, the value of R obtained from the experiment was equal to the one obtained by simulation. However, one range was offset from the other.

A sample simulation is shown in Figure 32. This is the case for a surface potential of 10.2 kV, a platform position of 55, and a beam energy of 9 kV. The abscissa is the deflection voltage used in the simulation and below it is drawn the scale of experimentally measured deflection voltages. Notice that the values of the V_1 and V_2 obtained by simulation are different from those obtained by experiment although their difference R is the same. This offset is due to slight misalignment in the experimental system and will not create any problem because the two ranges are matched. This offset problem was handled by adding a constant voltage to experimental data.

In Figure 32, the potential V(x) is shown by x's and the impact angle θ_{imp} is shown by o's. The secondary emission coefficient σ is

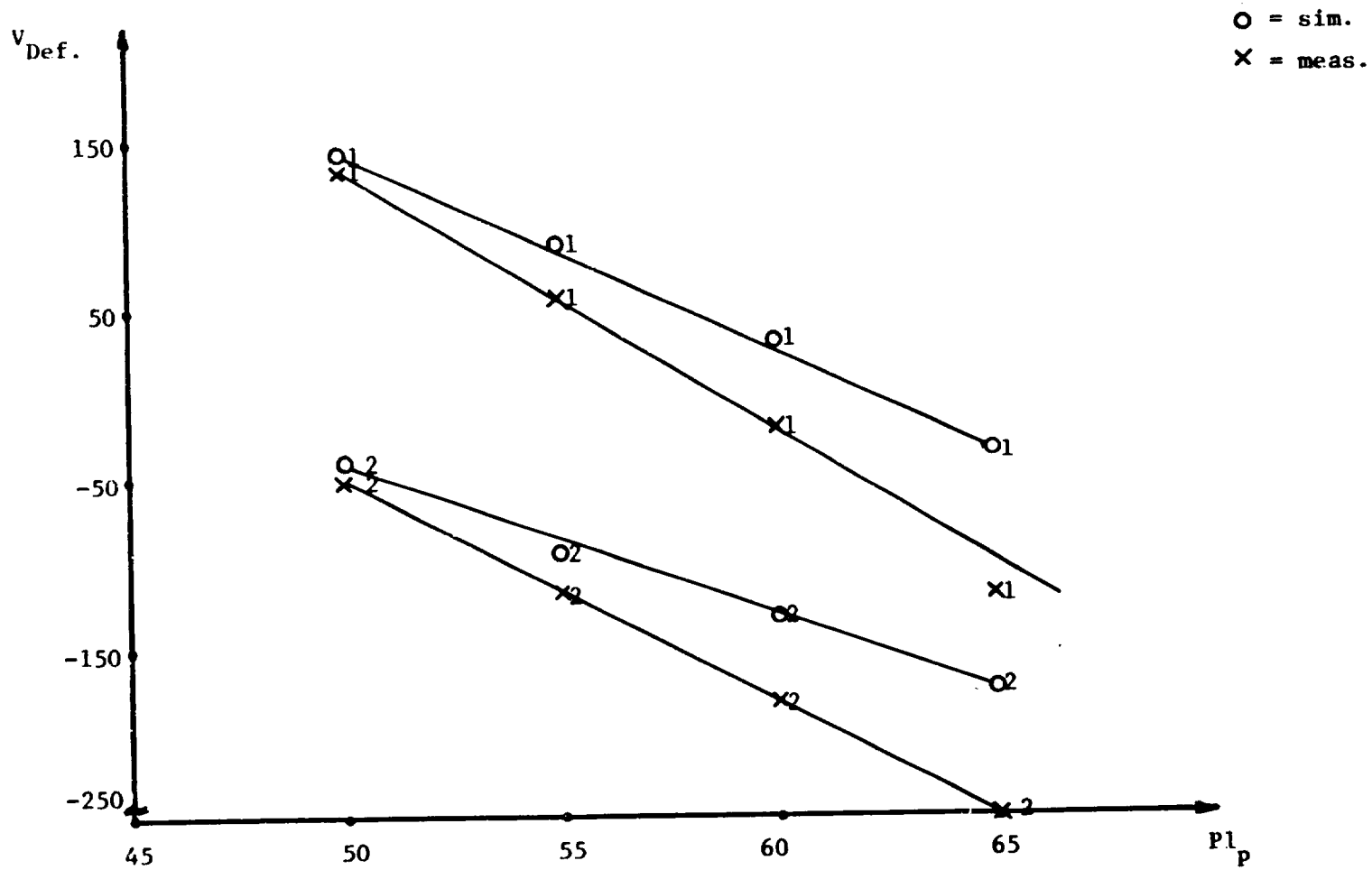

Figure 31. End points of range R´ vs. platform position pl_p.

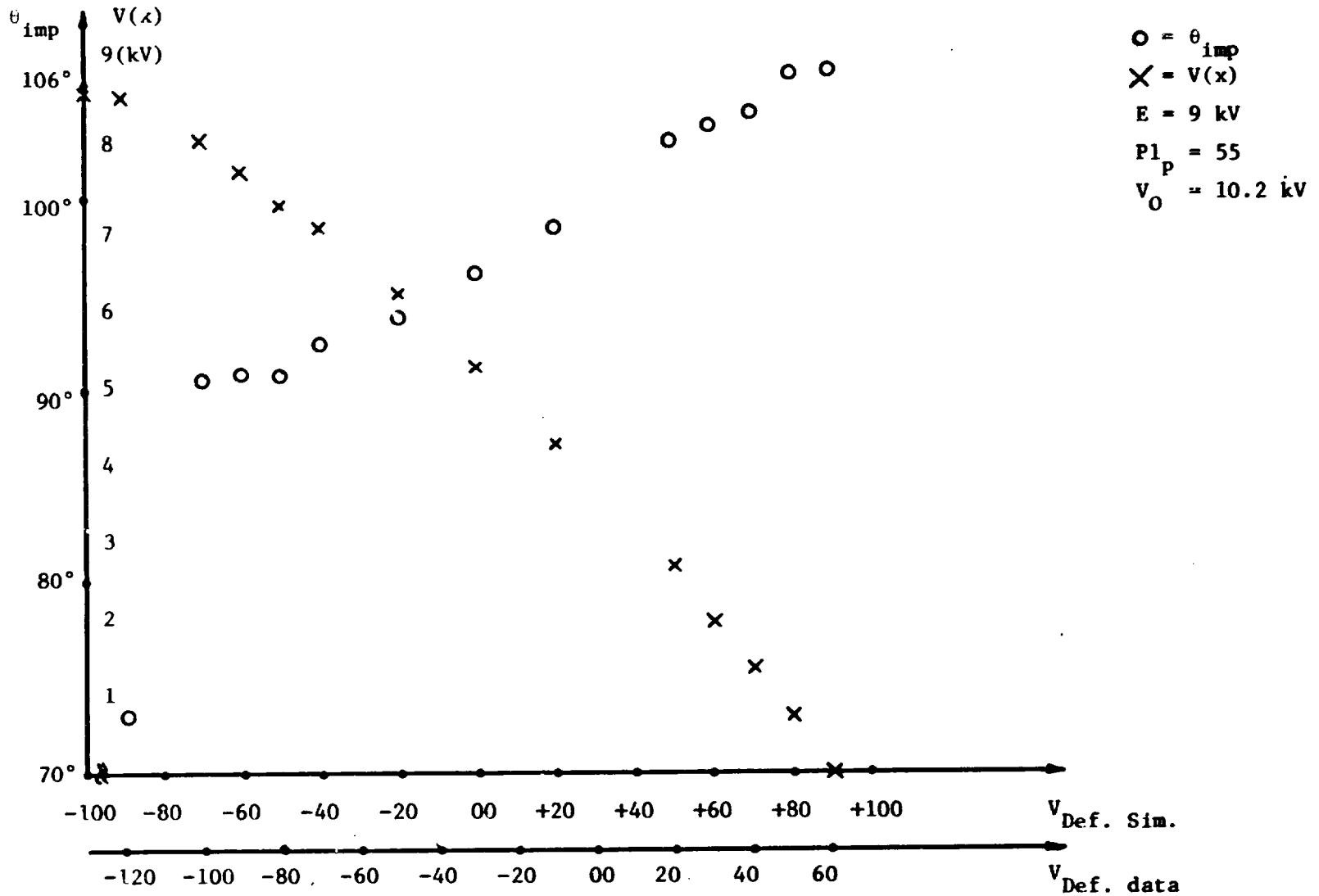

Figure 32. Plots of surface potential V(x) and impact angle θ_{imp} vs. simulated Deflection voltage. The measured deflection voltage is drawn on a lower scale.

found using this figure as explained below. For a given deflection voltage, the potential of impact point V(x) and its impact angle were obtained from the graph. The impact energy E_{imp} was calculated using

$$E_{imp} = E - V(x) \tag{57}$$

where E is the beam energy and V(x) is the potential of the impact point. The angle θ' is calculated as in Equation 54. Therefore, σ_{th} can be calculated as in Equation 29. Once this is done the two values of σ and σ_{th} are drawn vs. deflection voltage V_{Def} as shown in Figure 33.

Measurements were done for different platform positions and different energies with a surface potential of 10.2 kV. Data obtained from these measurements are plotted vs. impact energy and are divided into three different categories:

1. Low angle impacting particles with θ' between 0 and 20°.
2. Particles with angle θ' between 20° and 40°.
3. Particles with angle θ' above 40°.

Figure 34 shows the first case where $0 \leq \theta' \leq 20°$. This figure shows a collection of data for several different cases. Symbols × and ◇ show data for platform positions of 50, 55, 60 and 65. Note that the beam approaches the specimen obliquely when it leaves the gun. However, its trajectory is bent by the electric fields so that it approaches the specimen at normal incidence.

Figures 35 and 36 show the two other cases for $20° \leq \theta' \leq 40°$ and $40° \leq \theta' \leq 60°$. The abscissa is the impact energy. Note that the value of secondary emission coefficient measured for the case $40° \leq \theta' \leq 60°$ is higher than the two other cases because σ increases as θ' increases. The center surface potential for all three cases is 10.2 -kV.

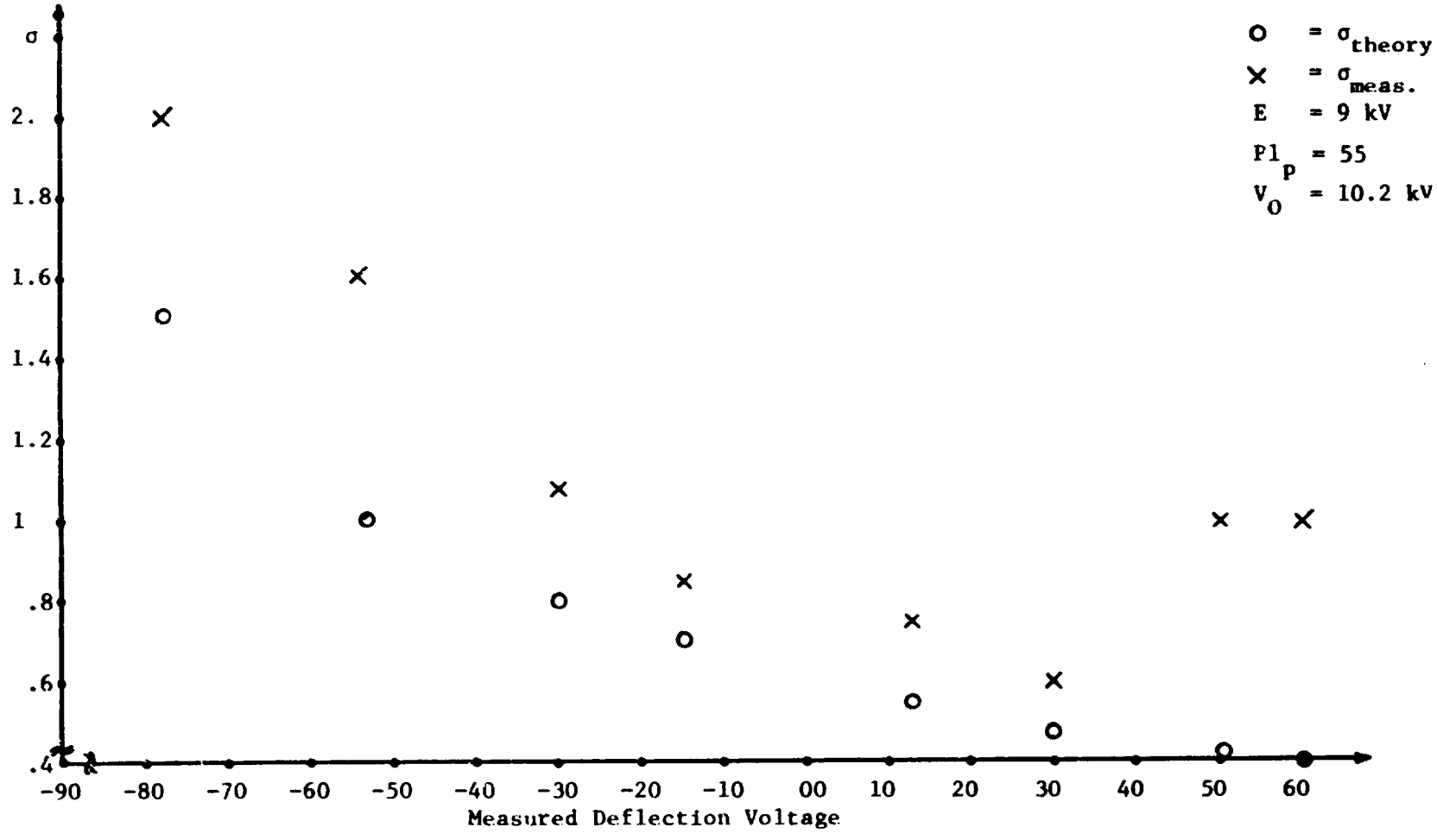

Figure 33. Plots of measured σ and σ predicted by the theory vs. deflection voltage.

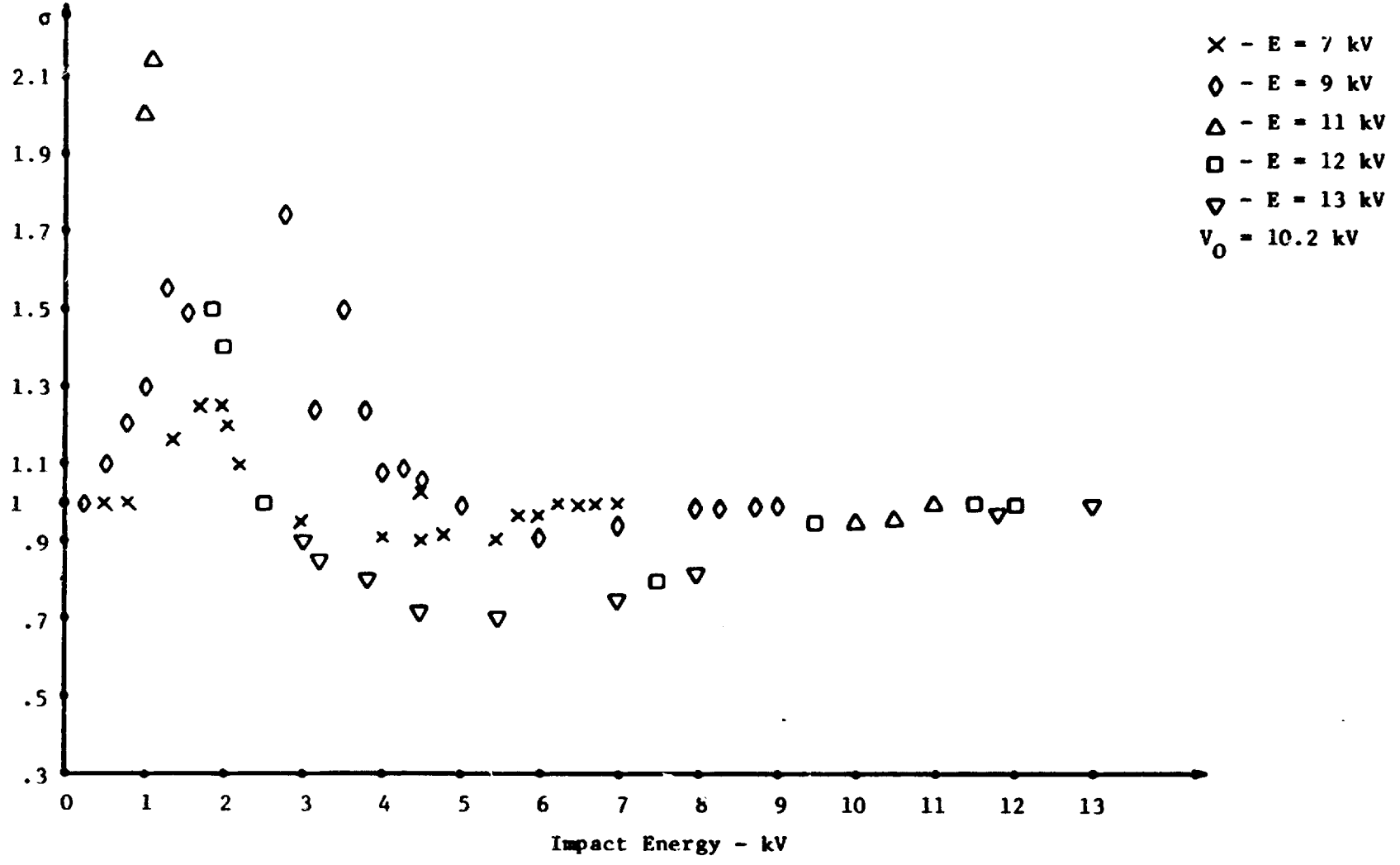

Figure 34. Plots of σ vs. impact energy for different beam energies. The angle of incidence θ´ is between 0° and 20°.

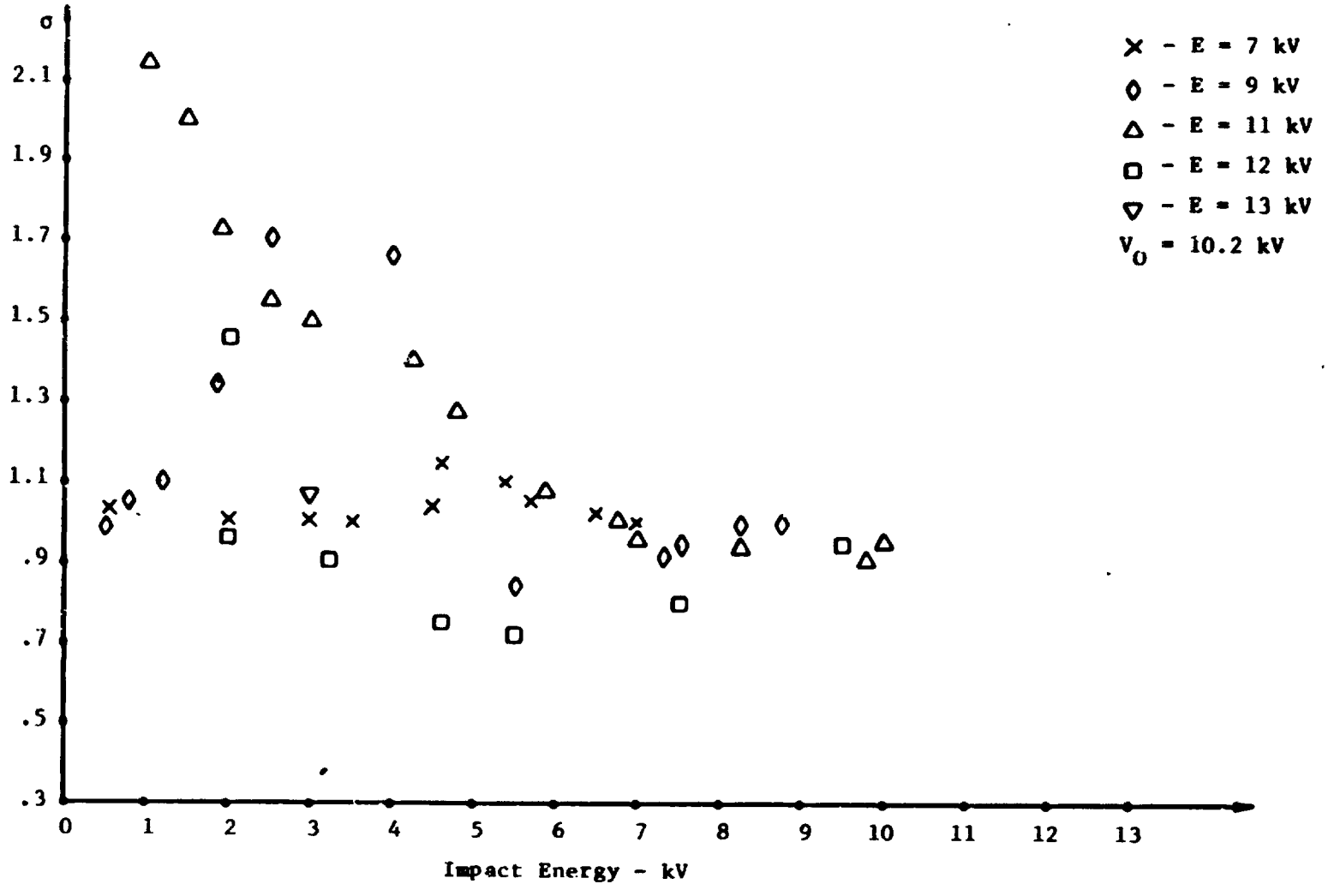

Figure 35. Plots of σ vs. impact energy for different beam energies. The angle of incidence θ is between 20° and 40°.

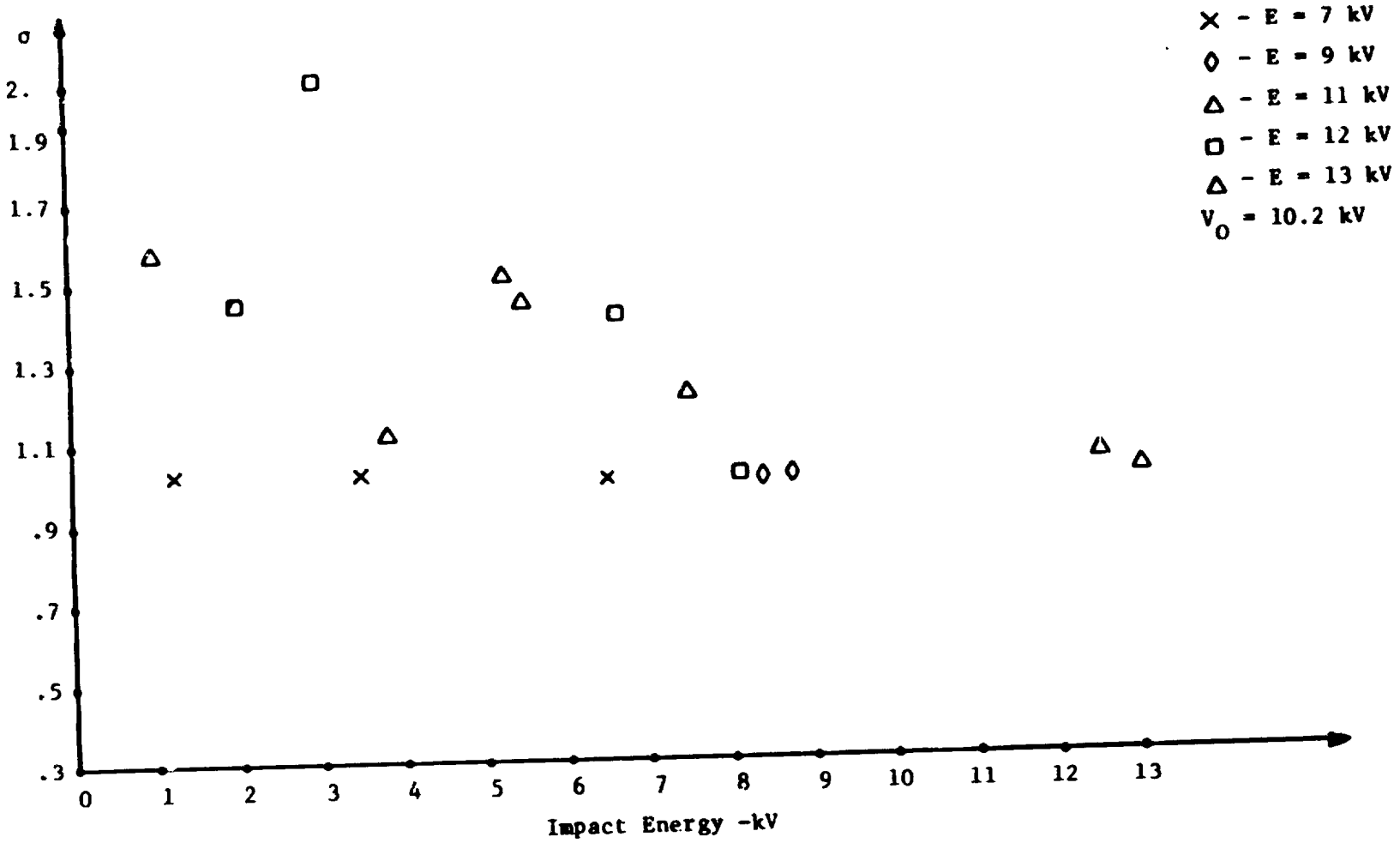

Figure 36. Plots of σ vs. impact energy for different beam energies. The angle of incidence θ´ is between 40° and 60°.

V. SECONDARY ELECTRON EMISSION IN PRESENCE OF ELECTRIC FIELD

Chapter V explains the effects of electric field on the secondary measurements conducted in this work. The electric field was normal near the center of the specimen and it was oblique around the edges of the specimen. This was due to the potential distribution on the surface of the specimen which was flat near the center and fell sharply around the edges. Curves of σ vs. impact point x and electric field vs. x are presented so that the reader can observe the difference in the values of σ in regions with normal and oblique electric field.

A. Electric Field on the Surface

The fields on the surface of the specimen were approximated by computer subroutines for various potential distributions(7). This routine required the points on the surface of the specimen to be specified in the calling statement and it calculates x-field and y-field. Figure 37 shows field distributions for a charged specimen having a 10.2-kV center surface potential and a polynomial of degree 4. Therefore, the potential distribution on the surface of the specimen is given by

$$V(x) = 10.2\ [1 - (x/3.17)^4]\ . \qquad (58)$$

Note that the field strength is a function of the exponent(7). A plot of normal field at the center of the specimen vs. the exponent is given in (7).

B. Measurements of σ Near the Edges (Oblique Field)

As mentioned earlier, because the potential falls to zero around the edges of the specimen, oblique fields exist near the edges. Some

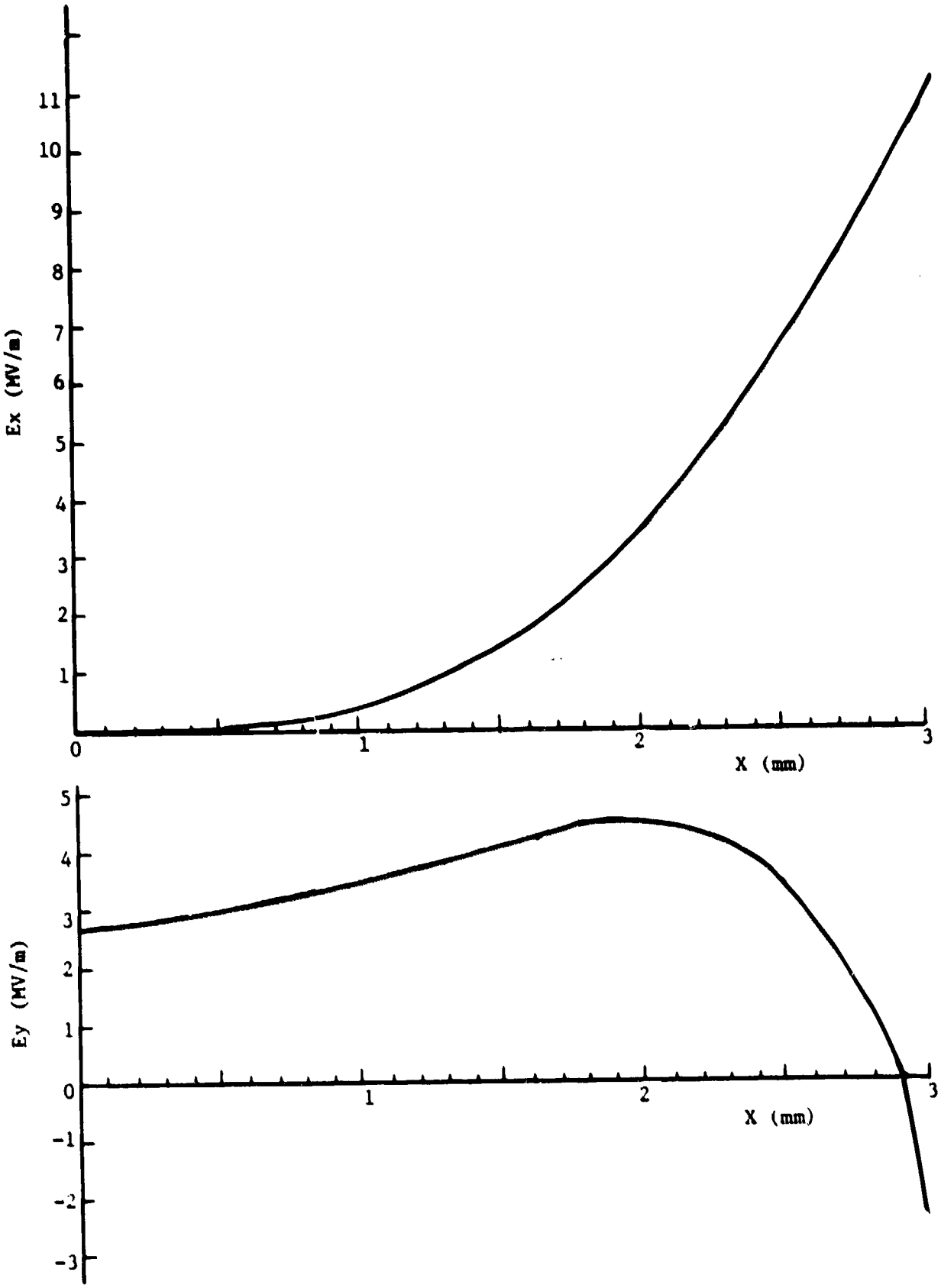

Figure 37. X and Y component of electric field on the surface of the specimen. X is in mm.

of the measurements described in Chapter IV were done in that region. For these the specimen was charged to a 10.2-kV center surface potential by procedure explained in Chapter II. Then the platform was set at position 50 so that it made a 90° angle with the horizontal plane. The beam energy was set at 7 kV or 9 kV so that the beam could only strike around the edges where the potential was low. Then, secondary measurements were done as explained in Chapter IV. This was repeated for platform positions of 55, 60 and 65. Note that each motor step corresponds to 1.8°. For the 7-kV cases, the beam struck the specimen at impact points $-3.17 \leq x \leq -2.4$, and for the 9-kV cases, the range was $-3.17 \leq x \leq -1.9$. Note that the beam struck the specimen at angles θ' ranging from 0° to 60°.

Plots of σ vs. X for the experimental data of Chapter IV are drawn in Figures 38, 39 and 40. These plots are divided into three categories as was done for the plots of σ vs. E_{imp}:

1. Low-angle impacting particles with θ' between 0° and 20°.
2. Particles with angle θ' between 20° and 40°.
3. Particles with angle θ' above 40°.

C. Measurements of σ in Regions with Normal Field

Other measurements described in Chapter IV were done near the center of the specimen where the field was normal (Figure 37). The specimen was charged to a 10.2-kV center surface potential and the platform was set at 27 which was the normal position. The beam energy was set at 11-kV so that it could hit the center of the specimen. The beam struck near the center of the specimen with almost normal angle and, as it was deflected near the edges, it struck obliquely. Secondary

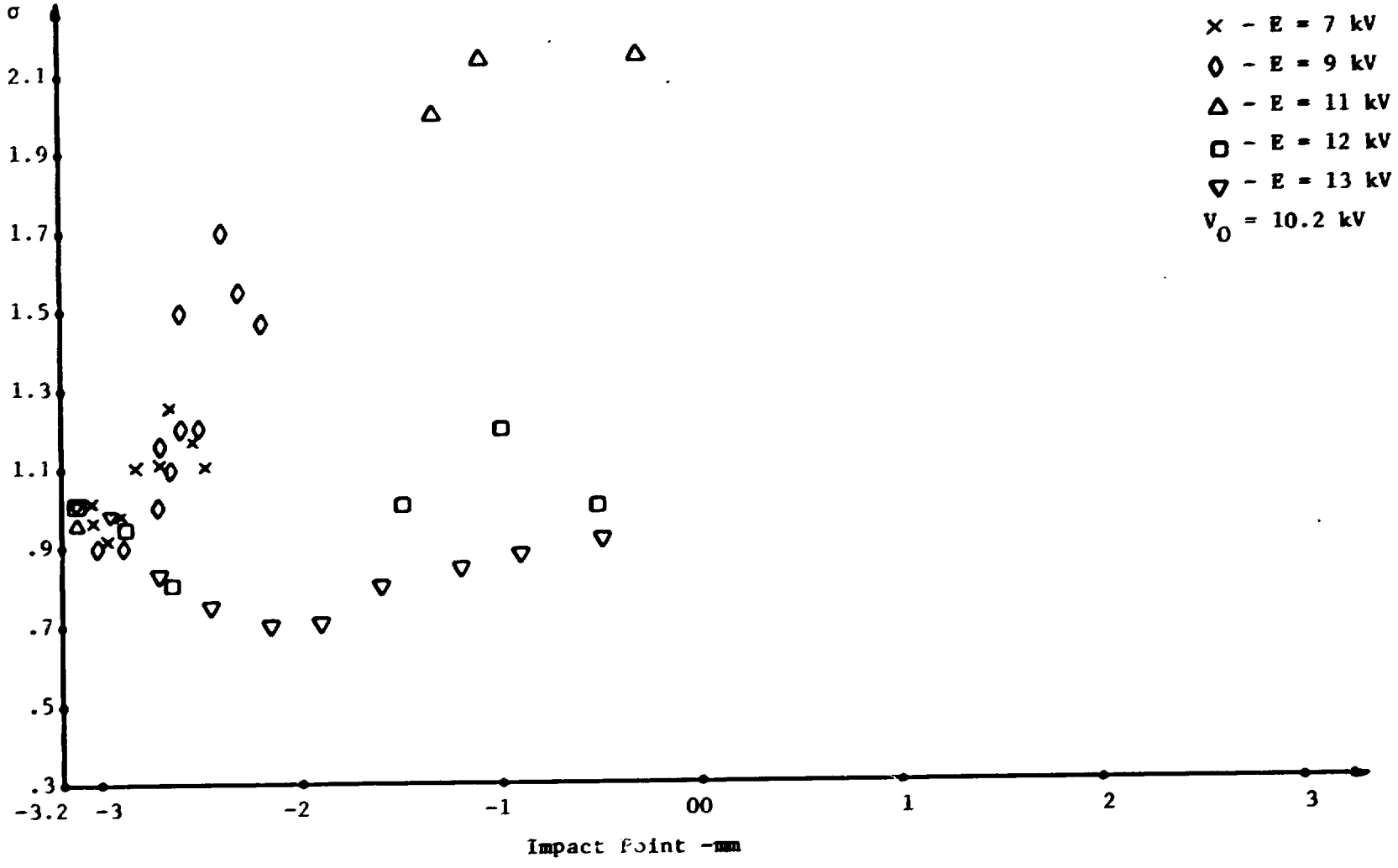

Figure 38. Plots of σ vs. impact point for different beam energies. The angle θ´ is between 0° and 20°.

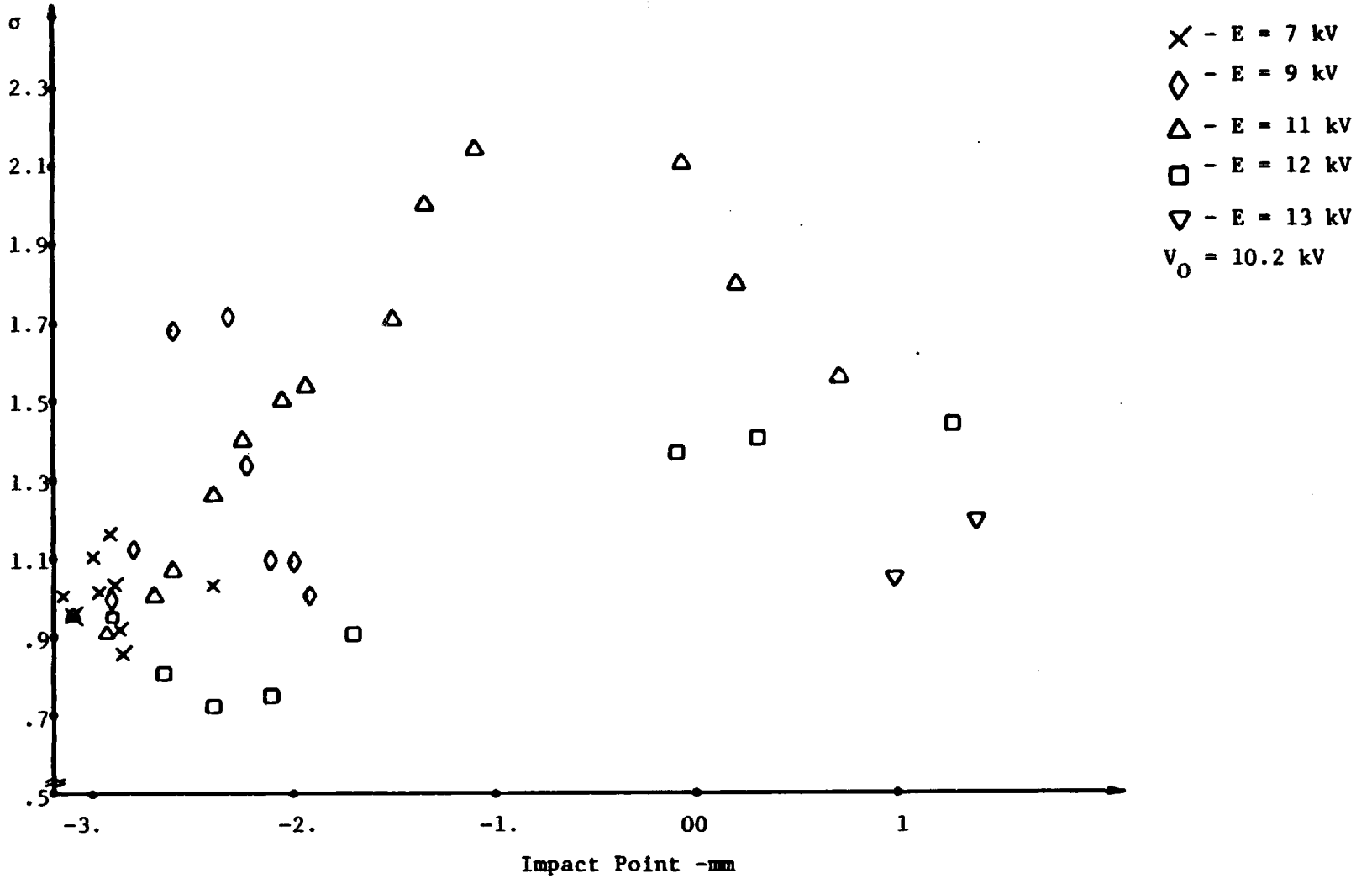

Figure 39. Plots of σ vs. impact point for different beam energies. The angle θ´ is between 20° and 40°.

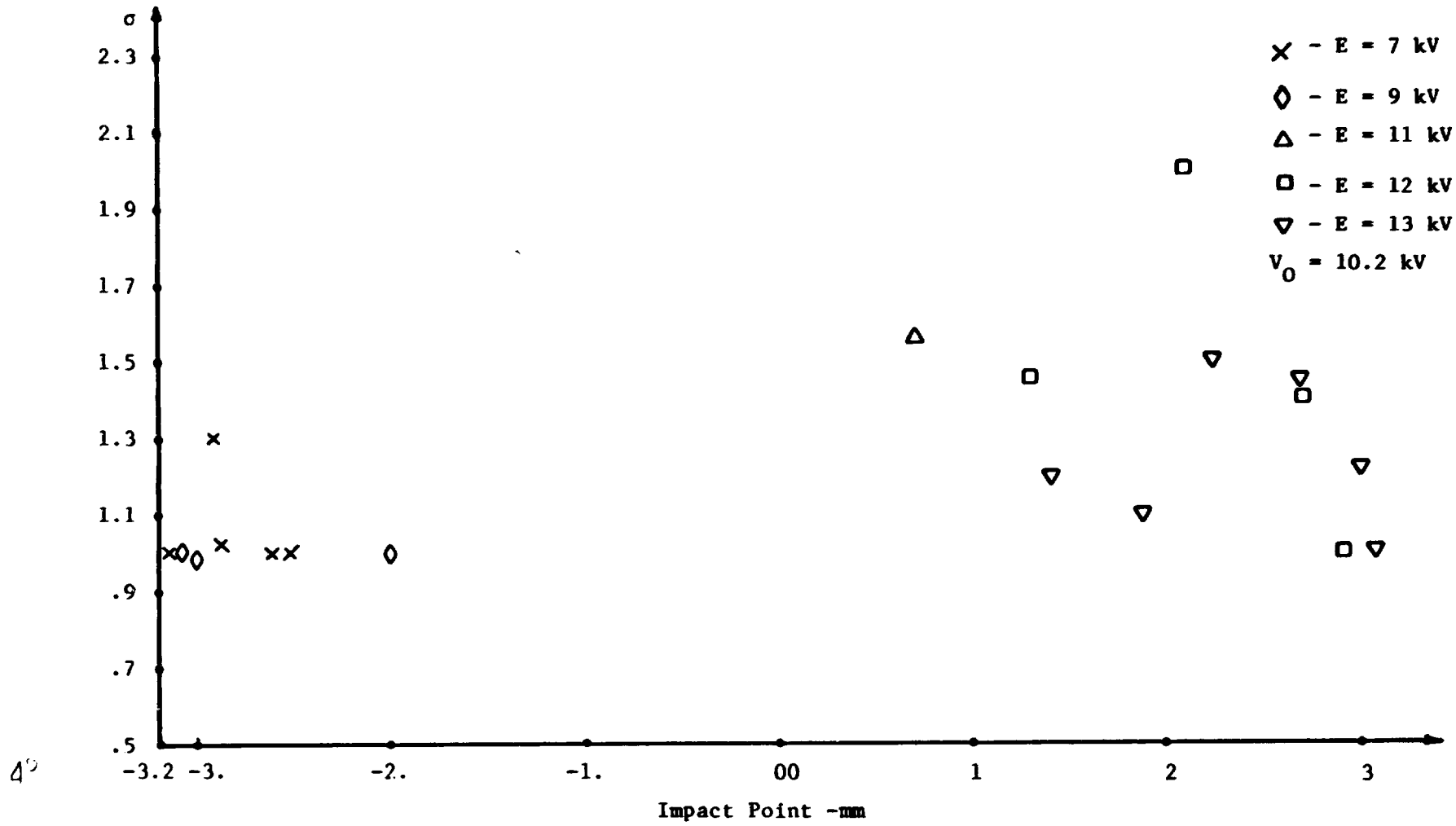

Figure 40. Plots of σ vs. impact point for different beam energies. The angle θ´ is between 40° and 60°.

measurements were done as explained in Chapter IV. More data was taken for the normal case by setting the beam voltage at 12 kV, 13 kV and 14 kV. The same experiment was done for platform position of 35 which is 14.6° tilted from the normal position with beam energies of 11 kV, 12 kV, 13 kV and 14 kV. The data taken for platform positions of 27 and 35 are also shown in Figures 38, 39 and 40. Note that in these cases, the beam struck all the points on the surface of the specimen. Therefore, data obtained from these cases were for both regions with normal and oblique electric field.

D. An Analysis of Experimental Procedures

In this section, the experimental procedure used to measure the secondary emission coefficient σ is analyzed. These procedures were completely covered in Chapter IV. The main issue is whether or not the measurements at the edges of the specimen and near where the beam is lost are reliable.

The collimated probe beam has a finite thickness of 0.15 mm, which means that at the edge of the specimen only a part of the beam is hitting the specimen and the other part is hitting the platform as shown in Figure 41. Thus the response shown on the electrometer Q_s is lower than what it is supposed to be. According to Equation 52 this will result in a σ closer to unity than it should be. Therefore, any measurement made at $X \leq -3.0$ or $X \geq 3.0$ is not reliable.

The same situation happens when the beam is striking the specimen with a grazing angle of incidence. In this case, only a part of the beam is hitting the specimen as shown in Figure 42. This might explain why all the experimental data have values very close to one at either end of the range as the plot shown in Figure 38 illustrates.

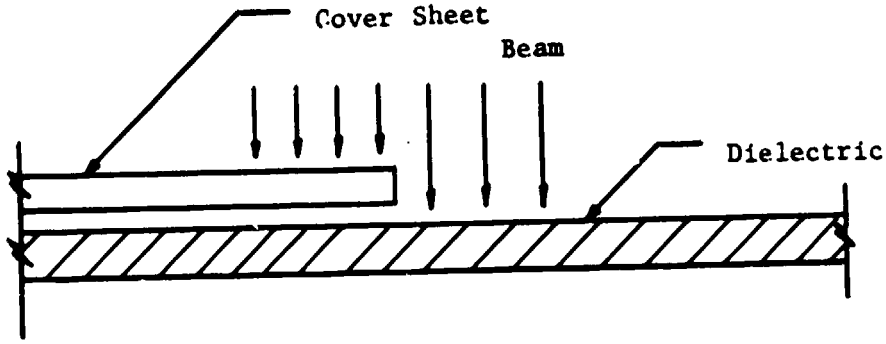

Figure 41. Representation of the situation when the beam is striking near the edge.

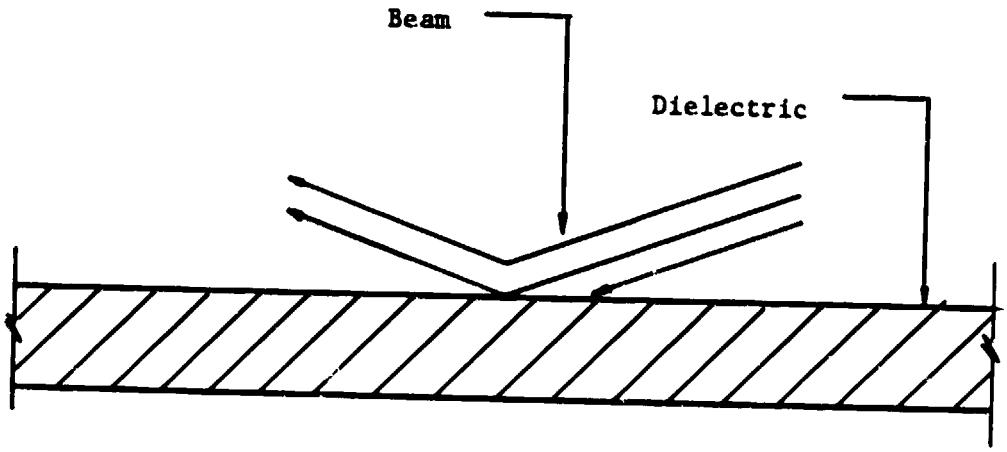

Figure 42. Representation of the situation when the beam is almost lost.

E. An Analysis of Measured Data

A careful study of plots of σ vs. either impact point X (figures 38, 39 and 40) or impact energy E_{imp} (Figures 34, 35 and 36) reveals some departures from the theoretical model which occur where the electric field is not normal to the specimen. For example consider the case of E = 13 kV in Figure 38. At the right-hand end of the curve, the secondary electron emission is one and it decreases as the beam approaches the edge. However, near X = 2 mm, the curve turns around and increases. This occurs in the presence of a high tangential electric field. The case of E = 13 kV and values of σ predicted by theory are shown in Figure 43. Therefore, the measured data in regions with high tangential electric field don't agree with the values of σ predicted by theory. Near the center of the specimen where the field is normal, a modified version of the theory can be used which accounts for the normal field by changing the critical energy E_c. Similar cases for different beam energies are observed in the figures mentioned earlier.

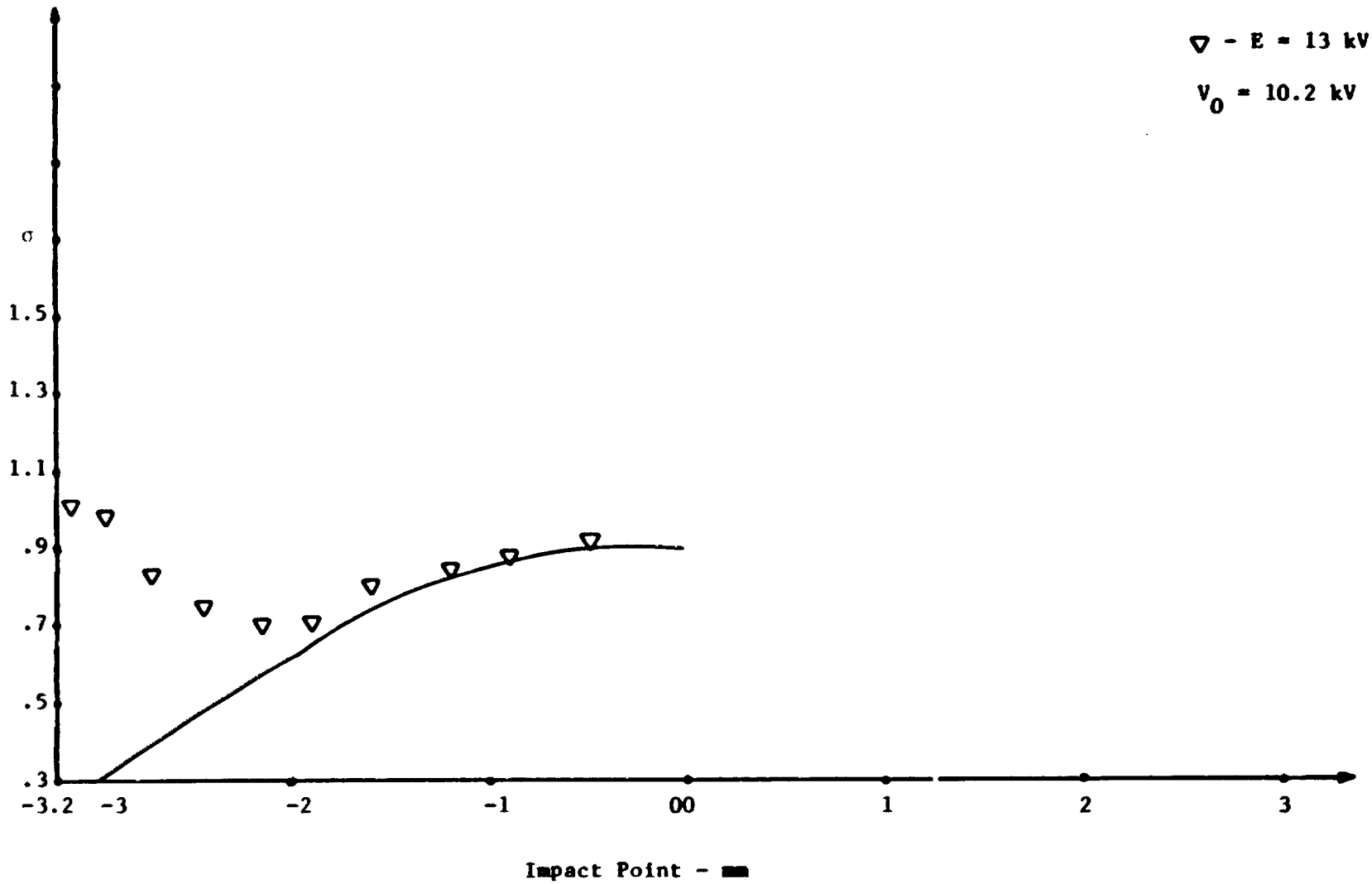

Figure 43. Plots of σ vs. impact point for experimental data and theory.

REFERENCES

1. Robinson, J. W. "Charge distributions near metal-dielectric interfaces before and after dielectric surface flashover," Proceedings of the Spacecraft Charging Technology Conference, 1977, AFGL-TR-77-0051, pp. 503-515, 24 February, 1977.

2. Robinson, J. W. "Surface charge kinetics near metal-dielectric interfaces exposed to kilovolt electron flux," Final Report, NASA Grant NSG-3097, September, 1977.

3. Robinson, J. W. "Mapping of electrical potential distribution with charged particle beams," Semi-annual Report, NASA Grant NSG-3166, July, 1979.

4. Robinson, J. W. and D. G. Tilley. "Potential mapping with charged particle beams, "Spacecraft Charging Technology, 1978, AFGL-TR-79-0082, pp. 606-620, October 31-November 1, 1978.

5. Tilley, D. G. "Dipole and quadropole synthesis of electric potential fields," Technical Report, NASA Grant NSG-3166, July, 1979.

6. Quoc-Nygen, N. "Secondary electron emission from a dielectric film subjected to an electric field," A Thesis in Electrical Engineering, November, 1977.

7. Robinson, J. W. "Mapping of electrical potential distribution with charged particle beams," Seni-annual Report, NASA Grant NSG-3166, September, 1980.

8. Budd, P. A. "Secondary electron emission from electrically charged Flourinated-Ethylene-Propylene Teflon for normal and non-normal electron incidence," A Thesis in Electrical Engineering, March, 1981.

9. Willis, R. F. and D. K. Skinner. "Secondary electron emission yield behavior of polymers," Solid State Communications, Vol. 13, pp. 685-688, 1973.

10. Dekker, A. J. Solid State Physics, Prentice-Hall, Inc., 1959.

11. Dobretsov, L. N. and M. V. Gomoyunova. Emission Electronics, Israel Program for Scientific Translations, Jerusalem (translated from Russian by I. Schechtman).

12. Salow, H. Z. Tech. Phys., 21, 8 (1940); Phys. Z., 41, (1940).

13. Lye, R. G. and A. J. Dekker. "Theory of secondary emission," Phys. Rev., Vol. 107, No. 4, Aug. 18, 1957, pp. 977-981.

14. Young, J. R. "Dissipation of energy by 2.5-10 keV electrons in Al_2O_3," Journal of Applied Physics, Vol. 28, No. 5, May 1957, pp. 524-525.

15. Young, J. R. "Penetration of electrons in aluminum oxide films," Physical Review, Vol. 103, No. 2, July 1956, pp. 292-293.

16. Kanter, H. "Energy dissipation and secondary electron emission in soilds," Physical Review, Vol. 121, No. 3, February 1961, pp. 677-681.

17. Bruining, H. Physica, Vol. 3, p. 1046, 1936.

18. Jonker, J. L. H. "On the theory of secondary electron emission," Phillips Research Reports, Vol. 6, pp. 372-387, 1951.

19. Jackson, J. D. Classical Electrodynamics, Wiley, 1962.

20. Bruining, H. Physics and Application of Secondary Electron Emission. McGraw-Hill Book Company, Inc., 1954.